

AFRL-RV-PS-  
TR-2016-0071

AFRL-RV-PS-  
TR-2016-0071

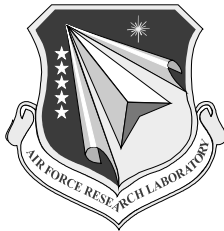
# INCORPORATION OF A GENERALIZED DATA ASSIMILATION MODULE WITHIN A GLOBAL PHOTOSPHERIC FLUX TRANSPORT MODEL

C. Nick Arge, et al.

31 March 2016

Final Report

APPROVED FOR PUBLIC RELEASE; DISTRIBUTION IS UNLIMITED.



**AIR FORCE RESEARCH LABORATORY  
Space Vehicles Directorate  
3550 Aberdeen Ave SE  
AIR FORCE MATERIEL COMMAND  
KIRTLAND AIR FORCE BASE, NM 87117-5776**

## DTIC COPY

## NOTICE AND SIGNATURE PAGE

Using Government drawings, specifications, or other data included in this document for any purpose other than Government procurement does not in any way obligate the U.S. Government. The fact that the Government formulated or supplied the drawings, specifications, or other data does not license the holder or any other person or corporation; or convey any rights or permission to manufacture, use, or sell any patented invention that may relate to them.

This report was cleared for public release by the PRS OPSEC Office and is available to the general public, including foreign nationals. Copies may be obtained from the Defense Technical Information Center (DTIC) (<http://www.dtic.mil>).

AFRL-RV-PS-TR-2016-0071 HAS BEEN REVIEWED AND IS APPROVED FOR PUBLICATION IN ACCORDANCE WITH ASSIGNED DISTRIBUTION STATEMENT.

//SIGNED//

---

Dr. C. Nick Arge  
Project Manager, AFRL/RVBXS

//SIGNED//

---

Glenn M. Vaughan, Colonel, USAF  
Chief, Battlespace Environment Division

This report is published in the interest of scientific and technical information exchange, and its publication does not constitute the Government's approval or disapproval of its ideas or findings.

# REPORT DOCUMENTATION PAGE

Form Approved  
OMB No. 0704-0188

Public reporting burden for this collection of information is estimated to average 1 hour per response, including the time for reviewing instructions, searching existing data sources, gathering and maintaining the data needed, and completing and reviewing this collection of information. Send comments regarding this burden estimate or any other aspect of this collection of information, including suggestions for reducing this burden to Department of Defense, Washington Headquarters Services, Directorate for Information Operations and Reports (0704-0188), 1215 Jefferson Davis Highway, Suite 1204, Arlington, VA 22202-4302. Respondents should be aware that notwithstanding any other provision of law, no person shall be subject to any penalty for failing to comply with a collection of information if it does not display a currently valid OMB control number. PLEASE DO NOT RETURN YOUR FORM TO THE ABOVE ADDRESS.

<b>1. REPORT DATE (DD-MM-YYYY)</b> 31-03-2016		<b>2. REPORT TYPE</b> Final Report		<b>3. DATES COVERED (From - To)</b> 01 Oct 2007 to 30 Sep 2015	
<b>4. TITLE AND SUBTITLE</b> Incorporation of a Generalized Data Assimilation Module within a Global Photospheric Flux Transport Model				<b>5a. CONTRACT NUMBER</b>	
				<b>5b. GRANT NUMBER</b>	
				<b>5c. PROGRAM ELEMENT NUMBER</b> 61102F	
<b>6. AUTHOR(S)</b> C. Nick Arge, Carl J. Henney, Josef Koller, W. Alex Toussaint, Humberto C. Godinez, Irene Gonzalez Hernandez, Kyle S. Hickmann, Alex Fay, David MacKenzie, Kathleen Shurkin, Eric K. Sutton, Stephen White, C. Rich Compeau, and Shawn Young				<b>5d. PROJECT NUMBER</b> 2301	
				<b>5e. TASK NUMBER</b> PPM00005114	
				<b>5f. WORK UNIT NUMBER</b> EF004379	
<b>7. PERFORMING ORGANIZATION NAME(S) AND ADDRESS(ES)</b> Air Force Research Laboratory Space Vehicles Directorate 3550 Aberdeen Avenue SE Kirtland AFB, NM 87117-5776				<b>8. PERFORMING ORGANIZATION REPORT NUMBER</b> AFRL-RV-PS-TR-2016-0071	
<b>9. SPONSORING / MONITORING AGENCY NAME(S) AND ADDRESS(ES)</b>				<b>10. SPONSOR/MONITOR'S ACRONYM(S)</b> AFRL/RVBXS	
				<b>11. SPONSOR/MONITOR'S REPORT NUMBER(S)</b>	
<b>12. DISTRIBUTION / AVAILABILITY STATEMENT</b> Approved for public release; distribution is unlimited. (OPS-16-10861 dtd 08 Apr 2016)					
<b>13. SUPPLEMENTARY NOTES</b>					
<b>14. ABSTRACT</b> The objective of this research effort was to improve significantly our ability to represent the instantaneous state of the global solar photospheric magnetic field distribution by incorporating advanced data assimilation techniques into a photospheric flux transport model. Prior to this work, all global photospheric magnetic field maps of the Sun were constructed using either simple magnetogram merging methods or from magnetic flux transport models that made use of either direct insertion or simple weighted averaging to update them with new observations. In addition, the new model was developed so that it could assimilate both near-side magnetogram and far-side helioseismically detected active region data so that truly instantaneous global solar photospheric magnetic field maps are generated. The photospheric flux magnetic flux transport model selected for this effort was the Worden and Harvey (WH) model originally developed at the National Solar Observatory. Along with the WH model, we incorporated the advanced data assimilation framework originally developed for radiation belt studies at Los Alamos National Laboratory (LANL). The main outcome of this research effort is the state-of-the-art data assimilative photospheric flux transport model now referred to as ADAPT (Air Force Data Assimilative Photospheric Flux Transport). The development of the ADAPT model significantly advances our ability to accurately specify the global photospheric magnetic field distribution, which serves as the primary input to solar and heliospheric models used by Air Force operations for space weather forecasting purposes.					
<b>15. SUBJECT TERMS</b> Solar, Photospheric Magnetic Fields, Magnetic Flux Transport, Data Assimilation, Helioseismology, Solar F10.7 Radio Flux, Solar EUV/XUV/FUV Irradiance, Solar Irradiance, Solar Wind, and Space Weather Forecasting					
<b>16. SECURITY CLASSIFICATION OF:</b>			<b>17. LIMITATION OF ABSTRACT</b>	<b>18. NUMBER OF PAGES</b>	<b>19a. NAME OF RESPONSIBLE PERSON</b> Dr. Charles N. Arge
<b>a. REPORT</b> Unclassified	<b>b. ABSTRACT</b> Unclassified	<b>c. THIS PAGE</b> Unclassified	Unlimited	64	<b>19b. TELEPHONE NUMBER (include area code)</b>

This page is intentionally left blank.

## Table of Contents

1. INTRODUCTION .....	1
2. BACKGROUND .....	1
2.1 Traditional Photospheric Magnetic Flux Synoptic Maps .....	1
2.2 Photospheric Flux Transport Models.....	2
2.3 Data Assimilation .....	2
2.4 Helioseismic Far-Side Imaging .....	3
3. METHODS, ASSUMPTIONS, AND PROCEDURES .....	5
4. RESULTS AND DISCUSSION .....	7
4.1 Year 1 .....	7
4.4.1 Worden and Harvey Model.....	7
4.1.2 Understanding NSO Magnetogram Data and Kalman Filter.....	8
4.2 Year 2 .....	9
4.2.1 The Worden Harvey (WH) Flux Transport Code .....	9
4.2.2 Integration of WH with LANL Ensemble Code .....	10
4.2.3 GONG .....	11
4.2.4 Intelligent Front End/Data Base.....	11
4.3 Year 3 .....	12
4.3.1 The Worden and Harvey (WH) Flux Transport code .....	12
4.3.2 LANL Data Assimilation Routine .....	12
4.3.3 Testing and Application of ADAPT .....	12
4.3.4 Preliminary WSA Results Using ADAPT Maps .....	14
4.3.5 WSA Modeled Coronal Holes Compared with STEREO EUVI Observations.....	15
4.4 Year 4 .....	16
4.4.1 LANL Data Assimilation Routine .....	16
4.4.2 WSA Solar Wind Model Comparison With STEREO B Observations .....	17
4.5 Year 5 .....	18
4.5.1 ADAPT Development.....	18

4.5.1.1 Detecting Far-Side Active Regions .....	18
4.5.1.2 Incorporating Far-Side Data into ADAPT .....	20
4.5.1.3 Parallelization of the LANL Data Assimilation Routine .....	21
4.5.2 Testing and Application of ADAPT .....	22
4.5.2.1 Forecasting F10.7 with ADAPT.....	22
4.5.2.2 Sources and Physics of F10.7.....	24
4.5.2.3 WSA Coronal & Solar Wind Predictions With & Without Far-Side Detected Active Regions Included.....	25
4.5.2.4 Ensemble Modeling of CME Propagation Using ADAPT .....	27
4.6 Year 6 .....	28
4.6.1 ADAPT Development.....	28
4.6.1.1 ADAPT Parallelization.....	28
4.6.1.2 New Monopole Removal Methodology .....	29
4.6.1.3 Increased Collaborative Feedback.....	29
4.6.1.4 LETKF Parallelization .....	31
4.6.2 The Helioseismic Far-Side Data .....	31
4.6.2.1 Far-Side Data Improvements.....	31
4.6.2.2 Far-Side Active Region Specification and Assimilation.....	33
4.6.3 Testing and Application of ADAPT .....	35
4.6.3.1 ADAPT EUV/XUV/FUV Forecasts .....	35
4.6.3.2 Integration of ADAPT Into WSA .....	37
4.7 Year 7 .....	39
4.7.1 Improvement in the Data Assimilation Methodology Used in ADAPT .....	39
4.7.2 Application of ADAPT Maps .....	42
4.7.2.1 Further Development of a Unique Method for Forecasting Solar EUV/XUV/FUV .....	42
4.7.2.2 Facilitating the Incorporation of ADAPT EUV Forecasts Into Ionospheric and Thermospheric Models .....	43
4.7.2.3 Global Impact of Far-Side Flux Emergence on Coronal and Solar Wind Models.....	44

4.7.2.4 ADAPT Driven Time-Dependent Modeling of the Solar Wind Using WSA+Enlil.....	46
4.7.2.5 Advanced Modeling of the Solar Corona Using ADAPT .....	47
5. CONCLUSIONS.....	48
REFERENCES .....	50

## List of Figures

1. Simple helioseismic holography .....	4
2. Construction of a far-side image.....	4
3. WH model evolved synoptic map (latitude vs. longitude) .....	8
4. SOLIS VSM Carrington map.....	8
5. Standard deviation of observation as a function of distance from the central meridian.....	9
6. Diagram of the recursive Kalman filter algorithm.....	10
7. Diagram of the general data flow and processing of ADAPT .....	11
8. Preliminary comparison between the observed mean polar magnetic field values from Mount Wilson Solar Observatory (MWO) and ADAPT .....	13
9. Global coronal field polarity at 5 Rs from the WSA model .....	14
10. STEREO A & B EUVI observations compared with WSA coronal hole predictions.....	15
11. Sample ADAPT map with the standard EnKF implementation .....	16
12. Solar wind speed predictions generated by WSA at STEREO B .....	18
13. Comparison between calibrated far-side seismic maps .....	19
14. Example of the initial “basic” polarity estimation method.....	20
15. Example of the new polarity estimation .....	21
16. Far-side merging example.....	21
17. The LETKF algorithm .....	22
18. Three month comparison between the 1-day & 3-day (+) forecast values from ADAPT .....	23
19. Skill score comparison between ADAPT F10.7 empirical model and standard forecasting models .....	23
20. Comparison between ADAPT modeled F10.7 forecasts with and without including far-side data.....	24
21. Preliminary reduction of 1 of the 7 fields that comprise the solar full-disk obs at 2.8 GHz ...	24

22. ADAPT photospheric magnetic field without far-side active region included.....	25
23. Solar wind speed observations from STEREO B vs. WSA predictions .....	26
24. Time series of the near-ecliptic solar wind parameters at 1 AU.....	27
25. Modeled polar mean values compared to observation, using NSO/GONG magnetograms as input .....	29
26. Modeled polar mean values compared with observation.....	30
27. Similar to Figure 26, but using a prototype monopole dampening method.....	30
28. Scatter plot of the magnetic-field strength.....	32
29. GONG far-side map .....	32
30. Example ADAPT .....	33
31. Comparison between the area of active regions and the areas of phase regions .....	34
32. Magnetic polarity tilt plotted against phase region tilt .....	34
33. Comparison between ADAPT model and Stan Band-9 (29-32 nm).....	36
34. Comparison between ADAPT combined model forecasts for Stan Band-9 and the observed values .....	37
35. Correlation values for each Stan Band.....	37
36. One assimilation step using ENLS assimilation .....	40
37. One step of the ETKF assimilation .....	41
38. Global F-peak electron density simulated by NCAR-TIEGCM .....	43
39. WSA coronal and solar predictions driven by an ADAPT photospheric magnetic field map	45
40. WSA+Enlil solar wind density in the ecliptic plane.....	47
41. Comparison of observed and simulated emission in the 171Å, 193Å, and 211Å lines of the AIA instrument aboard SDO .....	48

This page is intentionally left blank.

## 1. INTRODUCTION

The Sun's strong photospheric magnetic field plays a key role in the plasma physics of the solar atmosphere and thus significantly influences coronal and solar wind physics; it is also the sole large-scale physical observable readily measured from Earth or spacecraft. The photospheric magnetic field therefore plays a central role in virtually all coronal and solar wind models and thus accurate knowledge of its flux distribution is required to obtain reliable estimates of the state of the corona, heliosphere and by extension, the solar wind-magnetosphere interaction.

This report summarizes a seven-year Air Force Office of Scientific Research (AFOSR) supported 6.1 basic research investigation to improve significantly our ability to represent the instantaneous state of the global solar photospheric magnetic field distribution through the use of a flux transport model, rigorous data assimilation techniques, and recent developments in helioseismology. This was a multi-institutional, collaborative effort comprised of scientists and programmers from the National Solar Observatory (NSO), Los Alamos National Laboratory (LANL), and the Air Force Research Laboratory (AFRL) who led the overall effort. Key participants include C. Nick Arge (AFRL), Carl J. Henney (AFRL), Josef Koller (LANL), W. Alex Toussaint (NSO), Humberto C. Godinez (LANL), Irene Gonzalez Hernandez (NSO), Kyle S. Hickmann (LANL), Alex Fay (NSO), David MacKenzie (AER), Kathleen Shurkin (UNM), Eric K. Sutton (AFRL), Stephen White (AFRL), C. Rich Compeau (AFRL), and Shawn Young (AFRL).

The outcome of this long-term research project is the development of the Air Force Data Assimilative Photospheric Flux Transport (ADAPT) model, which is increasingly used for solar and space weather basic and applied research efforts. For example, ADAPT is scheduled to be transitioned to operations in the next few years at the National Centers for Environmental Prediction (NCEP) for both DoD (Air Force) and civil (e.g., National Oceanic and Atmospheric Administration (NOAA)) space weather forecasting purposes.

## 2. BACKGROUND

As stated in the Introduction, ADAPT is data assimilative photospheric magnetic flux model that uses both near-side magnetograms and also helioseismically derived far-side active region detections as its input. This section provides background and introductory material on traditional photospheric magnetic flux maps (i.e., what they are and how they are made), magnetic flux transport models, data assimilation, and helioseismology techniques for detecting and characterizing far-side active regions. It also provides descriptions of the flux transport model and data assimilation methodology originally used in ADAPT both of which have been significantly modified and improved since the beginning of this effort. Details of the specific changes and improvements made over the seven year span of this effort are described in detail in Section 4 of this report.

### 2.1 Traditional Photospheric Magnetic Flux Synoptic Maps

Since only half of the Sun can be observed from Earth at any given moment in time and the observational accuracy varies over the observable portion of the Sun, it requires approximately

27 days (i.e., the rotation period of the Sun as observed from Earth) to assemble global maps of the photospheric field distribution. For decades, the common approach for merging the magnetograms has been to use a peaked weighting factor that is a function of the longitudinal distance from the Sun's central meridian at the time of observation. In this method, the more reliable measurements made near central meridian are given the largest weight. Synoptic maps made in this manner are thus a time history of the line-of-site (LOS) magnetic field along the Sun's central meridian and are commonly referred to as Carrington maps. And, such maps have been constructed and used for more than 40 years (e.g., [1], [2], [3], [4], and references therein).

Another common approach for constructing synoptic maps has been to use the most recent magnetograms available from the last  $\sim$ 27 days of observations. These maps, referred to as updated solar synoptic maps, consist of the most recent  $360^\circ$  of LOS observations and have as their leading edges the eastern end of the most recent magnetogram added. These maps typically consist of observations from portions of two different Carrington rotations. Unlike Carrington maps, the magnetic field values of daily updated maps are made up of progressively fewer averaged magnetograms as one moves toward the eastern edge of the map, which means that the data on that edge are typically noisier and subject to projection effects. However, an advantage of an updated map is that the part of the map directed towards Earth consists of the most recent magnetic field observations available, especially east of the Sun's central meridian, making them useful (when used in the models) for providing the best estimate of the current configuration of the corona and heliosphere. Since we only see half of the Sun at any give time, we necessarily must use old observations (from the previous rotation) to fill those portions of the map currently not observable, which is a significant draw back. Another key drawback of Carrington and Updated synoptic maps is that space and time are mixed since any element of longitude represents the averaging of many magnetograms.

## 2.2 Photospheric Flux Transport Models

Flux transport models attempt to partially compensate for the problems intrinsic to traditional synoptic maps by evolving the magnetic flux on the Sun using relatively well understood transport processes occurring on the Sun (when observations are not available), such as meridional drift, supergranular diffusion, differential rotation, flux cancellation, and small scale random flux emergence. They update the model by incorporating new data into the calculations as they becomes available and thus help us to obtain a best estimate of the flux distribution on the Sun at any given moment in time. Because they cannot predict the emergence of new active regions (e.g., when they emerge on the backside of Sun), they must rely on frequent updating to compensate for this limitation. Flux transport models were first developed in the early 1990's [5] and a number of different versions, of varying sophistication, have been developed since then (e.g., [6], [7], [8], and references therein).

## 2.3 Data Assimilation

Data assimilation is the combination of physical models with observational data [10]. The purpose is to find the most likely estimation to the true state (which is unknown) using the information provided by the chosen physical model and the available data accounting for the uncertainties and the limitations of both.

Common approaches used in data assimilation involve Kalman or ensemble Kalman filtering techniques [9]. There are several advantages of using Kalman filter based data assimilation. First, all data (including their uncertainty) can be merged and then be combined with a physics based model accounting for its uncertainties. The Kalman filter gives one a framework for easily including multiple data sources whenever they are available and when this is a reasonable thing to do. In principle, data from multiple sources can be used and not necessarily restricted to be from one ground or space based instrument. Adding data from multiple sources is, in principle, straightforward, though calibration differences can make this rather challenging. The data can be extrapolated into data empty regions in a manner that is consistent with the model forecast and the observations at the same time. Second, all uncertainties are carried along such that each estimate or forecast also includes an uncertainty [10]. Third, past regional correlations are automatically accounted for, and fourth, data assimilation can be used to compensate for absent physics in the model [11].

The ensemble Kalman filter is in turn based on a Monte Carlo method that can simultaneously estimate the state of a physical system and model parameters. It is a powerful method that can use any physical model in the form of a black box (see, e.g., [9] for a review). This makes the data-model framework modular where the physics model can be easily replaced and more data can be added without requiring many changes.

The principle of the Kalman filter is described below. It is often initialized with a best guess or climatology model. It then recursively calculates new forecasts iterating over the following three steps:

1. It calculates a weighting factor called the Kalman gain based on observations and their uncertainty.
2. It adjusts the magnetic field to match the observations using the Kalman gain.
3. It produces a new forecast that can then be compared to observations

The Kalman filter can also be used to gain insight into model parameters by combining a model with a historical data set. The meteorological community has termed such an approach as “reanalysis”. This provides one with more information about the model, its deficiencies and forecast capabilities because data assimilation gives one the tools to effectively compare data with model forecasts and assess where the model would be drifting away if no data were assimilated.

## 2.4 Helioseismic Far-Side Imaging

For the past decade helioseismic acoustic holography, a technique developed by Lindsey & Braun [12 &13], has been used to map magnetic regions on the non-visible disk of the Sun. Since its first application in 2000 to SOHO/Michelson Doppler Imager data [14], the method has proven to be uniquely capable of detecting large active regions on the solar far-side. It also allows for the tracking of active regions around the far-side for many days before the sunspots are facing the Earth and possibly producing space weather.

As its name implies, acoustic holography is based on the interference of sound waves that can be used to create a sonic image of a feature below the photosphere in a manner analogous to optical holography. Figure 1 illustrates a simple case of helioseismic holography. In the left panel, two subsurface sources radiate acoustic waves in all directions. Some of the waves intersect the surface, where their interference pattern is observed. The temporal and spatial variations of this interference pattern can be filtered to isolate waves with particular characteristics, such as a sampling depth or focal plane. The filtered waves are then mathematically time-reversed using a model of the solar structure so that the structure of the sources at the focal plane can be recovered, as seen in the right panel of Figure 1. The focal plane can be placed at any depth, including the far-side of the Sun, by changing the filtering of the waves.

The detection of far-side active regions is inferred from observations of acoustic waves on the earth-facing front side of the Sun. The waves are filtered to isolate those that reflect on the solar far-side, bounce from another portion of the solar surface, and then reach the front side. The location of the front-side analysis areas, called pupils, are moved in order to place the focal point of the waves at different spatial locations on the far side, as shown in Figure 2. These waves exhibit a phase shift when a strong magnetic field is present at the reflection point on the solar far side. The phase shift is negative, indicating that the wave has taken less time to travel along its path, and suggesting that the underlying physical mechanism is an increase in the depth of the reflection point caused by the thermal effects of the magnetic field.

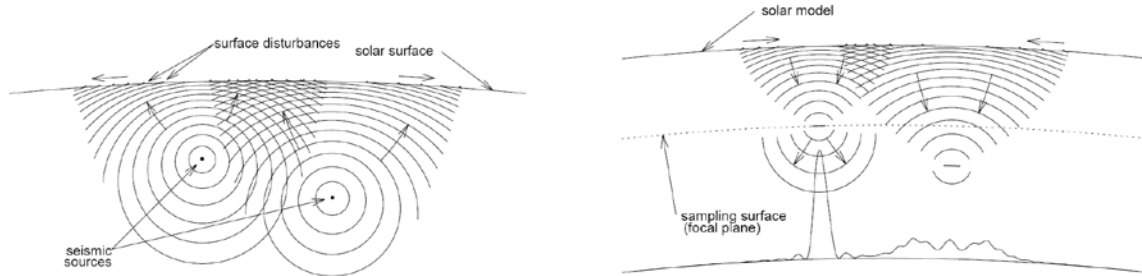


**Figure 1. Simple helioseismic holography.** In the left panel, two subsurface sources radiate acoustic waves in all directions. The curve in the right panel shows the recovered acoustic source strengths as a function of location for the chosen focal plane.

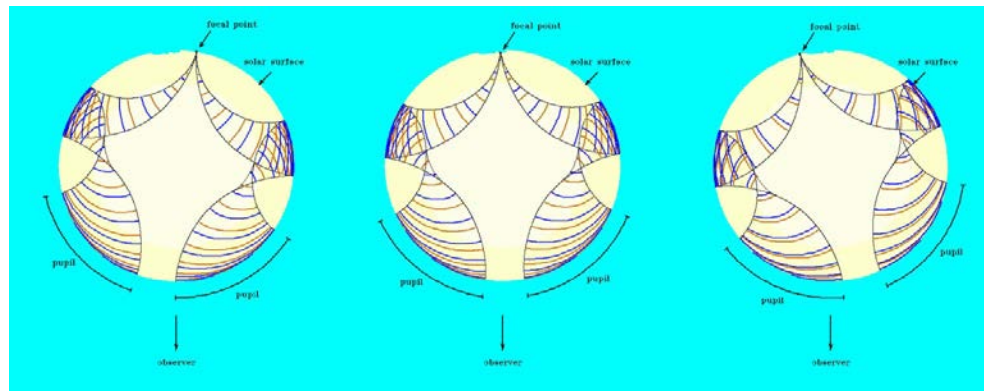


**Figure 2. Construction of a far-side image.** In the left panel, the focus is placed at a point to the right of an active region, shown as depression on the solar surface. In the central panel, the focus point is on the active region, and in the right panel the focus point is to the left of the active region. The temporal phase of the waves propagating towards and away from the focal point is shifted by the presence of the active region.

The spatial coverage of the far side depends on the number of bounces or “skips” that the filtered waves undergo as they propagate through the Sun. Figure 2 depicts a so-called 2x2-skip path that can sample the center of the far-side disk, but cannot probe near the limbs. This outer area is provided by filtering the data for waves that follow a combination of (1x3)-skip and (3x1)-skip paths, and then combining the two sections of the far-side disk with a smoothing function. The area of overlap has a somewhat lower sensitivity to activity. Continuous full-hemisphere far-side maps have been calculated from Global Oscillation Network Group (GONG) data since 2005. Far-side phase shift signatures have been parameterized in terms magnetic field strength [15]. The relationship between the far-side phase shift,  $\phi$ , and the magnetic field strength,  $B$ , is

$$\phi = \phi_1 \ln (1 + B^2/B_0^2) \quad (\text{Eq. 1})$$

where  $\phi_1 = (-1.41 \pm 0.03) \times 10^{-2}$  radians and  $B_0 = 9.46 \pm 0.57$  gauss. Inverting Eq. 1 gives the following expression for  $B$ :

$$B = B_0 (\exp(\phi/\phi_1) - 1)^{1/2} \quad (\text{Eq. 2})$$

Thus, it is possible to produce a far-side magnetic synoptic map with a quantitative estimate of the surface magnetic field, but without polarity information.

The subsequent sections present a summary of the activities conducted for this project. Section 3 outlines the main approaches originally proposed to develop a data assimilative photospheric flux transport model (now known as ADAPT) that ingests both near and far side observations. Section 4 summarizes progress made and results obtained for each year of the seven year effort. Concluding remarks are presented in Section 5.

### 3. METHODS, ASSUMPTIONS, AND PROCEDURES

The Worden and Harvey (WH) [6] magnetic flux transport code was selected for this effort. The WH model takes into account the following known processes occurring on the Sun between periods of new observations:

1. Differential rotation of the sun, where regions near the equator rotate more rapidly than at the poles. The Snodgrass formulation [16] is used to calculate this.
2. Solar meridional flows, which are  $\sim 10 \text{ m s}^{-1}$  pole-ward drifts of magnetic flux in each hemisphere, using the Wang and Sheeley [17] approximation for this transport process but with a smaller peak drift, as Worden and Harvey [6] find that it gives better agreement with observations.
3. Effects due to supergranular diffusion, which are horizontal flows of order 300 m/s within supergranules with the flows directed toward the supergranular cell boundaries. To mimic this effect, they use the random attractor method [18, 19], which tends to “clump” the magnetic flux together much as observed [6].
4. Random replenishment of the quiet-Sun magnetic flux.
5. Updating of the evolved global magnetic field map with new observations as they become available. Since the uncertainties in the observations get larger as one approaches the limb of the Sun, a center to limb cutoff radius is determined (based on the how noisy the data are).

Typically it is located at an angular distance of about  $75^\circ$  from disk center. Observations beyond this point are not incorporated into the evolved map. Observations East of central meridian are directly spliced into the map, while those West of central meridian are smoothly merged in with the evolved values. Since the Sun is tilted  $7.25^\circ$  with respect to the ecliptic, each pole is filled with direct observations for about a third of a year when a given pole is directed maximally toward Earth. Due to the curvature of the Sun, one is effectively at the limb at  $\sim 83^\circ$ . Each pole is filled exclusively via the flux transport process for the rest of the time.

Both simple and advanced data assimilation techniques were integrated with the Worden and Harvey [6] photospheric flux transport model using a framework developed by Koller et al. [11] for their radiation belt study at Los Alamos National Laboratory (LANL). The LANL framework is based on the ensemble Kalman filter technique which was developed for use in terrestrial weather predictions [20]. At the start of this effort, all flux transport models, including the Worden and Harvey [6] model, updated the modeled field with new observations through a combination of direction insertion and simple weighted averaging. While this method is simple and fast it does not properly account for the observational/model uncertainties nor does it account for regional correlations. These deficiencies are corrected with the use three different of data assimilation methodologies. The first and most commonly used is the Ensemble Least Squares (ENLS) estimation method [21], which takes into account both model and data errors but does not consider spatial correlations. The second method used is the traditional Ensemble Transform Kalman filter (ETKF) method. It is a recursive algorithm that automatically takes into account past correlations between different regions of the photosphere. The third and final method used is the Local Ensemble Transform Kalman Filter (LETKF) method [22]. LETKF is a localized version of the ETKF. It was explored because it was discovered that the ETKF method drew erroneous long-distant correlations because of the small ensemble sample sizes used to estimate the ADAPT model covariance structure.

A final major aspect of this research effort was to develop methods for characterizing and then incorporating helioseismic far-side active region data from NSO/GONG into the ADAPT model. The helioseismic acoustic holography method used to detect sunspots on the far-side of the Sun (summarized in Section 2) is sufficiently sensitive to locate the positions and determine the magnitudes of the magnetic fields in large active regions. Adding these unique and key measurements to ADAPT complemented the earth-side magnetograms already being assimilated resulting in truly global solar photospheric field maps. As data assimilation requires specification of both the uncertainties of the measurements as well as in the model, the project investigated the best way to estimate the uncertainties of the far-side data. It also included developing and selecting the best methods for incorporating far-side data into global magnetic maps using rigorous data assimilation methods.

A requirement to make use of the far-side observations was to expand on the inferred far-side parameters so as to estimate the most probable polarity and orientation of the far-side fields. To accomplish this, known distributions of sunspot polarity, the Hale rule, and orientation, Joy's rule, for a given solar cycle and latitude were incorporated. Hale's rule for active regions is that between the solar hemispheres sunspots have opposite leading magnetic polarities, switching each solar cycle (e.g., [23]). Joy's rule for active regions is that the centroid of leading polarity is

closer to the equator than the following polarity (e.g., [24]). The best method to include these observed polarity rules, and accurately represent the observed distribution and uncertainties, within the model ensemble needs to be developed.

Throughout this effort, ADAPT generated maps were routinely used in models of the corona and solar wind in an effort to test whether where they improved specification and forecasts of the global corona and solar wind. In addition, new applications of ADAPT were explored and developed such as the discovery that the F10.7 radio flux and EUV emission could be forecasted using photospheric magnetic flux maps generated by ADAPT. Findings from these efforts are also described and summarized in Section 4.

## 4. RESULTS AND DISCUSSION

In this section, the progress and results achieved during each year of this effort are summarized.

### 4.1 Year 1

The research effort in year one focused on two main areas:

1. Getting the Worden and Harvey photospheric magnetic flux code working and delivered to AFRL Kirtland AFB.
2. Understanding the NSO (SOLIS & GONG) magnetogram data and beginning work to build the Kalman filter.

#### 4.1.1 Worden and Harvey Model

One of the initial milestones of the project was to revive the Worden and Harvey (WH) flux transport model developed by Dr. John Worden and Dr. Jack Harvey [6] at NSO. This code stopped running in early 2000 and remained unmaintained until early 2008. The WH flux transport code was debugged at NSO/Tucson in order to get the code working again. Date string handling errors were found and corrected in the IDL version of the WH model. In addition, the IDL code was modified to utilize SOLIS VSM longitudinal magnetograms, and the first set of evolved magnetic synoptic maps was created. Figure 3 illustrates an evolved synoptic map (latitude vs. longitude) using six months of SOLIS VSM data. Figure 4 is the SOLIS VSM Carrington map for the same solar rotation date (though in sine latitude). Comparison between the two maps illustrates the difference of including flux transport processes.

The WH model, originally developed in IDL, was translated into C, which is the version that was integrated with the data assimilation code. The new C version was modularized, documented and parameter metrics for WH model feedback were included. In addition, the new C version began to be modified so that it could make use of NSO GONG and KPVT magnetograms, which span the period from 1977 until present. Both IDL and the latest C version of WH code were successfully delivered to AFRL Kirtland Air Force Base and installed on computer systems there.

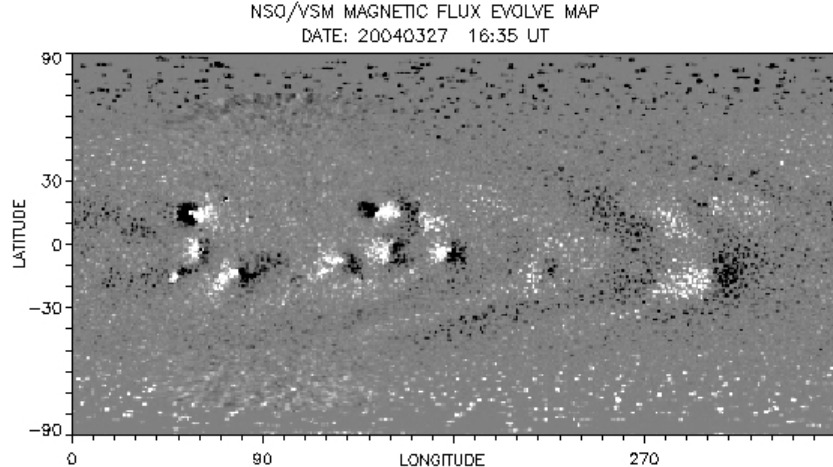


**Figure 3. WH model evolved synoptic map (latitude vs. longitude).**

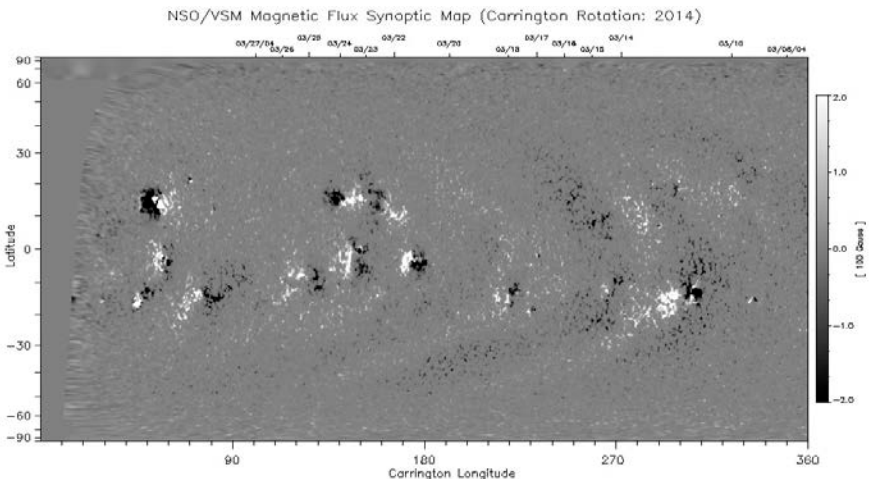


**Figure 4. SOLIS VSM Carrington map. For the same solar rotation date (though in sine latitude) of Figure 3.**

#### 4.1.2 Understanding NSO Magnetogram Data and Kalman Filter

Both NSO SOLIS and NSO GONG magnetograms were examined for structure and applicability as input to the data assimilation routine. GONG Janus-style magnetograms were identified as the input data of choice for several reasons. GONG has six observatories, yielding high probability of an observation when seeing conditions may be adverse elsewhere. The Janus-style maps are available with a 60-minute cadence, which is a good time step for the Kalman filter. Also, the Janus-style maps have an unmerged data field, consisting of averages from simultaneous observations, which can be easily extracted and used as input.

The Kalman filter's error covariance matrix requires quantification of observational variance. A simple estimate of the variance was constructed by examining the differences between simultaneous GONG images from four different observatories. Analysis showed that the variance more than doubled from the center to the limb, indicating that a more detailed analysis was necessary. Fortunately, GONG is able to have up to four simultaneous observations due to the geographic placement of its observatories. Over 100 magnetograms of such instances were

obtained and work was performed to calculate the variance as a function of distance from the subearth point. The uncertainties of the flux observations were then calculated because they are an important ingredient for the data assimilation. Standard deviation was calculated as a function of the central meridian, and as expected, it was found to increase with distance from that point (see Figure 5).

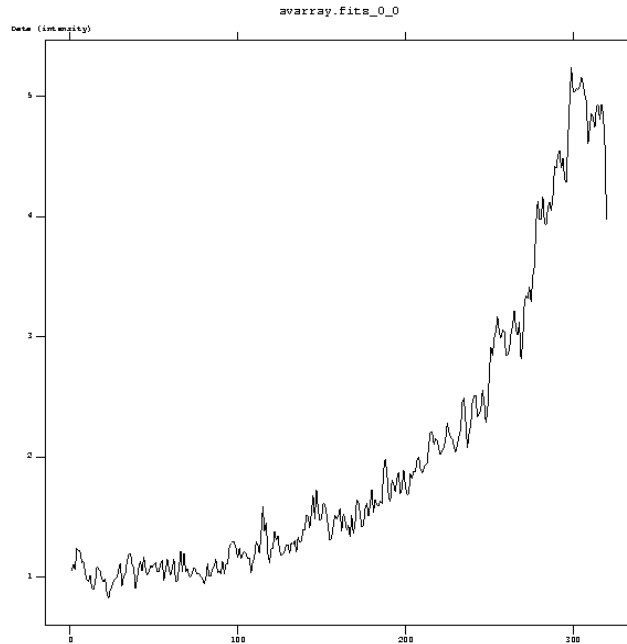


**Figure 5. Standard deviation of observation as a function of distance from the central meridian.**

## 4.2 Year 2

The research effort in year two focused on four main areas:

1. Making the Worden and Harvey (WH) Code more robust and flexible.
2. Integrating WH and the LANL data assimilation framework.
3. Using high cadence GONG magnetograms to estimate magnetic field variance.
4. Development of a methodology to retrieve the most reliable magnetograms.

### 4.2.1 The Worden Harvey (WH) Flux Transport Code

Significant effort went into making the WH modified code much more robust, flexible, and most critically, capable of fully interfacing with the LANL data assimilation framework. It was more thoroughly modularized and generalized to allow for model ensemble I/O and processing needed with the addition of the Kalman filter. The modified code was tested much more thoroughly and began to utilize an ensemble of model realizations using different model parameters constrained by the estimated errors of each parameter. In addition, the modified version allowed for the hemispheres to be decoupled with regards to differential rotation and meridional flow. The ensemble of flux transport models estimates the model error required by the LANL data assimilation framework. The flux transport parameters of the WH model are expected to vary

with the solar activity cycle. For example, the rotation rate of the small-scale background magnetic features varies with the solar cycle. The data assimilated synoptic map ensemble is saved for each time step, with a maximum cadence of 24 hours. For solar cycle parameter analysis, the plan was to use the ensemble to select the best set of model parameters for periods during the past 30 years. Finally, work began to verify that the new version of the WH model (i.e., the version that was translated from the original IDL into C) generated output equivalent to that produced by the original WH flux transport model.

#### 4.2.2 Integration of WH with LANL Ensemble Code

The Los Alamos data assimilation module was successfully implemented in the C version of the Worden-Harvey model. The data assimilation module is based on the ensemble Kalman filter method, which is used in many engineering and scientific applications including terrestrial weather predictions (see Figure 6). The ensemble Kalman filter is a Monte Carlo method that can simultaneously estimate the state of a physical system and model parameters. Initially the Kalman Filter code that was implemented was designed to be easy to read (by a human). However, it was soon realized that for very large grid numbers in the model being developed (360x180=64800) the size of the error covariance matrix P is very large and difficult to handle ( $64800^2 * 4$  bytes = 15.6 Gigabytes – too large even for modern high-performance computers). It was thus decided to rewrite the Kalman filter algorithm to minimize the actual computer memory requirements without reducing the accuracy of the Kalman filter. Evensen [9] published a numerical scheme for accomplishing data assimilation with large data grids. The memory requirements are reduced by a large factor and the largest matrix in memory is now only 64800 x 50 (typical ensemble size) corresponding to about 12 MB. The new ensemble Kalman filter was successfully implemented in this way.

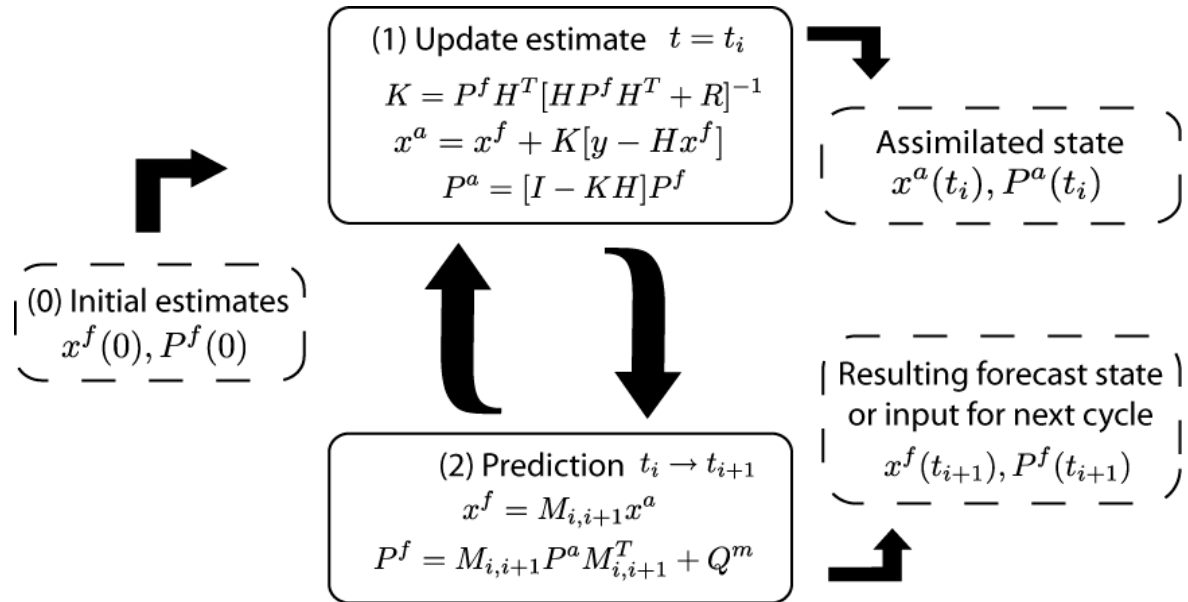


**Figure 6. Diagram of the recursive Kalman filter algorithm, which combines observations and model forecasts consistently across a global computational domain. Model and data uncertainties are included and carried along in the error co-variance matrix.**

Work to better understand the implications of the ensemble Kalman filter began. Model and observational uncertainties had to be accurately represented because the results strongly depended on them. In year two, the model uncertainties were represented by the spread of the ensemble members, which are created by a variation of flow velocity parameters. It was realized that the model uncertainty is grossly underestimated especially when a new active region is emerging at the limb. To address this problem, an additional model uncertainty was applied to represent a larger model error when the discrepancy between forecast and observations (for e.g. new active regions) was large. The much larger model uncertainty was used on a pixel-by-pixel basis. In addition, different model error representations began to be explored.

A scaled down version of the ensemble Kalman filter to neglect all cross-correlations was implemented. This assumption allowed for a simple least-square method to be applied. The model uncertainties were, again, implemented with the spread of the forecast ensemble members with the additional model error inflation. The forecast and observations are combined with a simple weighted mean with the weights inversely proportional to the variance.

### 4.2.3 GONG

One of the key elements required by data assimilation methods are estimates of the uncertainties in data to be assimilated. With photospheric magnetic field data as provided in magnetograms one can normally only estimate these uncertainties (e.g., by conducting variance studies using past data along with the assumption that the results realistically represent the data for all times), since in the past (e.g., with KPVT) magnetograms are only taking once or a few times a day. However, at the request of this project's development team, the NSO/GONG group began adding variance information as part of their 10 minute magnetogram data product.

### 4.2.4 Intelligent Front End/Data Base

A preliminary Intelligent Front End was pursued to select the best magnetograms from multiple instrument sources of the past 3 decades (see Figure 7) [25]. Work began to develop a MySQL magnetogram and photospheric field map data base for the ADAPT model, which allowed for more efficient handling of the numerous magnetograms produced by GONG and used by ADAPT.

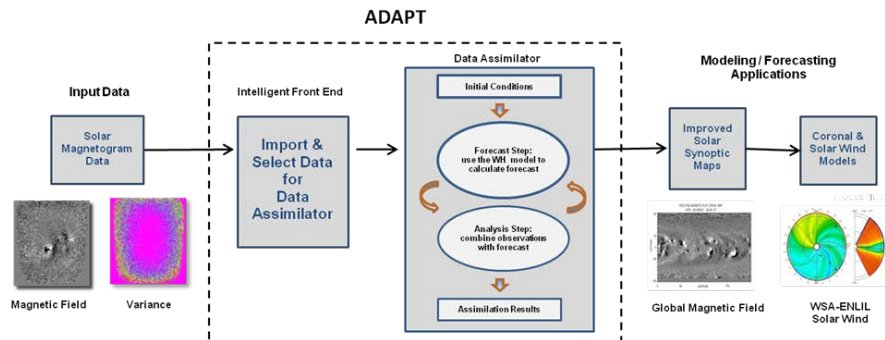


**FIGURE 7. Diagram of the general data flow and processing of ADAPT: The Intelligent Front End imports and selects the best available magnetogram data, along with estimated uncertainties, to be assimilated by the LANL ensemble Kalman filter with the latest WH flux transport map of the global solar magnetic field. These maps are then used as input for coronal and solar wind models, e.g., WSA-ENLIL [26].**

## 4.3 Year 3

The research effort in year three focused on three main areas:

1. Improvement in the Worden and Harvey (WH) flux transport code.
2. Application of the Los Alamos National Laboratory (LANL) Data Assimilation routine.
3. Testing and application of what is now referred to as the Air Force Data Assimilative Photospheric flux Transport (ADAPT) model.

### 4.3.1 The Worden and Harvey (WH) Flux Transport Code

In year three, key modifications were made to the WH flux transport part of the code. Specifically, the changes involved how supergranular diffusion is modeled. For sub-daily cadence, the previous WH supergranular diffusion method behavior resulted in flow patterns that had the potential to change abruptly. The new method utilizes a continuously varying spatial array that minimizes sudden changes and naturally evolves into slowly changing flow patterns. The new method made it less likely for there to be abrupt changes in the supergranular behavior over a small time step resulting in naturally evolving flows that are entirely independent of the initial pattern. The modifications also fixed noted flow bias near the poles such that every pixel now has an equal chance of being attracted in any possible direction, regardless of its latitudinal position. Additional modifications made to the model included: (1) a function to include new magnetic flux emergence regions by increasing the model variance when using the Ensemble Least-Squares data assimilation method, (2) the addition of an MySQL database function calls to replace a previous test-based input data file list resulting in faster run-time, And (3) a routine was developed that shifts the ADAPT maps from a fixed 0-to-360 degree Carrington frame to placing the central meridian of the last magnetogram added at the center of the map. This allows for direct comparison of WSA model coronal predictions with STEREO EUVI observations.

### 4.3.2 LANL Data Assimilation Routine

The ensemble least square filter technique was further improved. The method gave significantly better results than the traditional data merging method originally used in the Worden-Harvey model. The method applied was a standard weighted least-square method [21] combined with an ensemble description. The model and data error were described with ensemble perturbations and with model forecasts and observations combined locally. The ensemble spread was limited to 1-sigma deviation from observed flow values resulting in the sharpening of the forecast model spread. The model error is estimated dynamically from the variance of the ensemble at each time step.

### 4.3.3 Testing and Application of ADAPT

Preliminary model validation analysis began with ADAPT by comparing different model parameter output individually with observations (e.g., solar polar field observations and coronal holes) so as to provide feedback that helped determine the magnitude and time dependent

behavior of large scale magnetic flow patterns such as the meridional drift rates in each hemisphere.

One key metric for model parameter feedback is the evolution of the polar magnetic field. Measurements of the line-of-sight field near the Sun's poles are often highly unreliable because of their close proximity to the limb and because the Sun's rotation axis is inclined  $7.25^\circ$  to the ecliptic plane. Field measurements at the solar limb are difficult because only a small component of the field vector is directed toward the observer. This is further complicated by the highly variable horizontal magnetic field signal [27], which becomes increasingly prevalent near the limb. In addition, the observed tilt of the Sun from Earth has the effect of rendering one of the poles unobservable for months at a time.

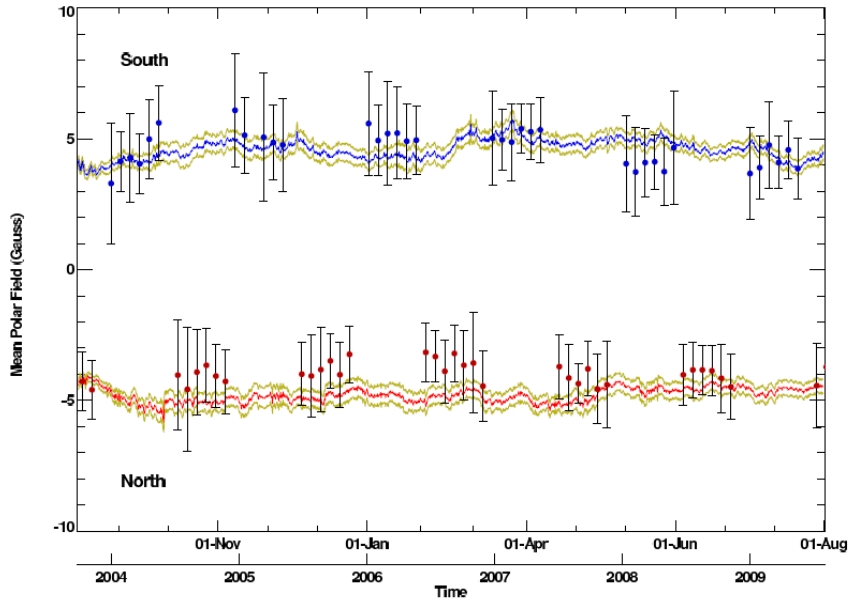


**Figure 8. Preliminary comparison between the observed mean polar magnetic field values from Mount Wilson Solar Observatory (MWO) magnetograms (dots) with 1-sigma error bars and ADAPT (lines) mean ensemble values. The blue (upper) & red (lower) dots and lines are from the south & north polar bands respectively. The upper and lower yellow lines illustrate the 1-sigma model error for the mean values determined from the ensemble.**

Flux transport models such as ADAPT overcome this problem by incorporating key transport processes (i.e., meridional drift and supergranular diffusion) that fill the poles naturally with magnetic flux from lower latitudes. New ADAPT validation functions were created to provide polar metric parameters for comparison with observation. The polar comparison seen in Figure 8 shows a preliminary comparison between Mount Wilson Solar Observatory (MWO) measurements of the polar fields when they are well observed (colored dots with associated error bars) and the field values at the poles as determined by ADAPT (colored solid lines). This result was very encouraging and demonstrated that the model can remain consistent with observations for extended periods of time.

#### 4.3.4 Preliminary WSA Results Using ADAPT Maps

WSA results were compared using global magnetic maps from ADAPT and standard Carrington as its input. As shown in Figure 9, the photospheric field distribution seen in the two input maps (Figures 9b and 9e) are significantly different from one another. In comparing the standard photospheric field Carrington map on the left with the corresponding ADAPT map on the right, it is evident that they differ more and more as one moves toward their right-hand edges. The maps are similar on their left sides because this is where the data have been recently merged into both the maps. The right side of the maps is located on the far-side of the Sun where no new traditional magnetogram data are available. The two maps differ so significantly here because the ADAPT model has evolved the fields using the WH flux transport process, while this is not done in standard Carrington maps and the fields are as they were when they crossed central meridian several days in the past.

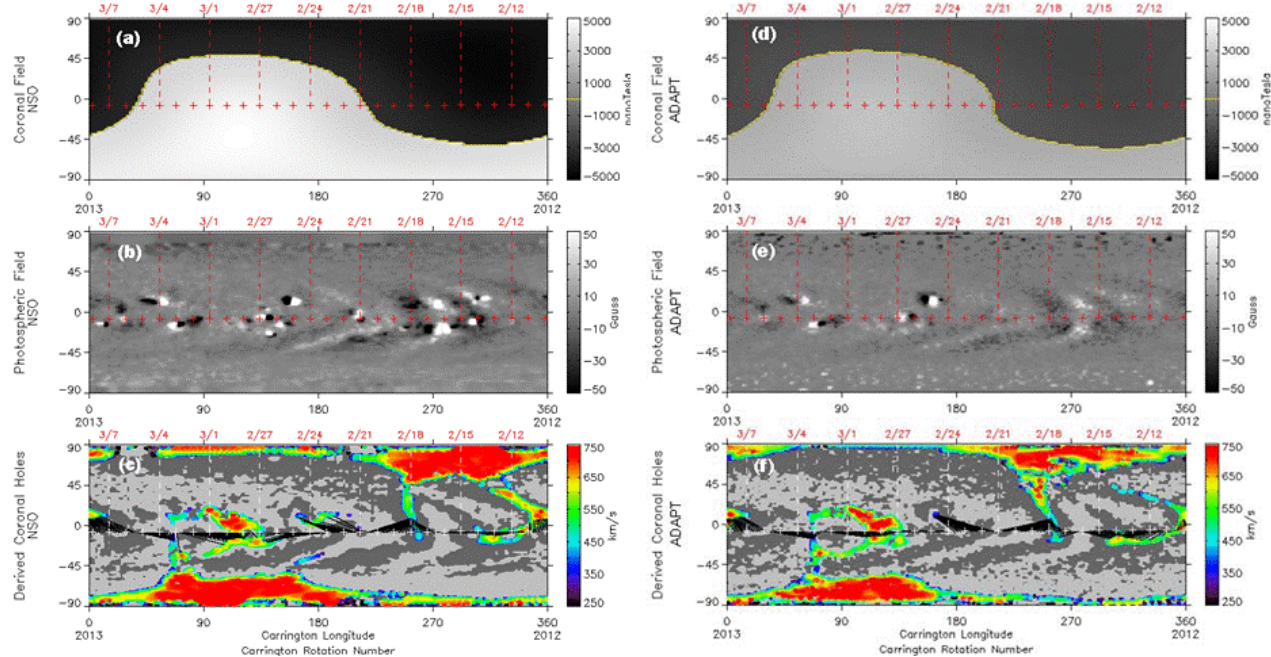


**Figure 9.** Global coronal field polarity at 5 Rs from the WSA model (a & d) using a National Solar Observatory (NSO) Carrington map (b) and an ADAPT map (e) as input. Outward (Inward) directed field indicated by white (black) areas. The red (or white in c & f) plus signs near the equator mark the daily positions of the sub-earth point. (c & f) Coronal holes as determined by the WSA model. The field polarity at the photosphere is indicated by the light/dark (positive/negative) gray contours, while the colored dots identify the foot-points of the open field lines at the photosphere. The dot color indicates the solar wind speed at 5.0 Rs as predicted by the model. The black straight lines identify the connectivity between the outer (open) boundary located at 5.0 Rs and the source regions of the solar wind at the photosphere (1.0 Rs).

The maps seen in Figures 9a and 9d are the radial magnetic field on a spherical surface positioned high (5 Rs) in the corona as determined by the Wang-Sheeley-Arge (WSA) model [28]. There are only subtle morphology differences between the two maps, but the field tends to simplify significantly high up in the corona. Figures 9c and 9f show the coronal holes (colored dots) as predicted by the WSA model. Substantial differences are evident in the sizes, shapes, and positions of the open field regions (coronal holes) even on the left side of the maps where the input maps to the model are most similar. Coronal holes are major sources of the solar wind and these results clearly demonstrate that traditional Carrington maps do not produce the same

coronal structure as that obtained using a more realistic, instantaneous snapshot of the global photospheric field distribution.

#### 4.3.5 WSA Modeled Coronal Holes Compared with STEREO EUVI Observations

The orbital configuration of the two STEREO spacecraft in year three (2010) was such that, in combination, they provide a nearly instantaneous global snapshot of the Sun's coronal hole distribution. This provided a unique opportunity to directly compare these data with WSA coronal hole predictions using both ADAPT and standard updated photospheric field maps as input to WSA. Such comparisons were made with the assistance of a University of New Mexico graduate student/Summer AFRL Space Scholar so that WSA modeled coronal holes could readily compared with STEREO EUVI observations.

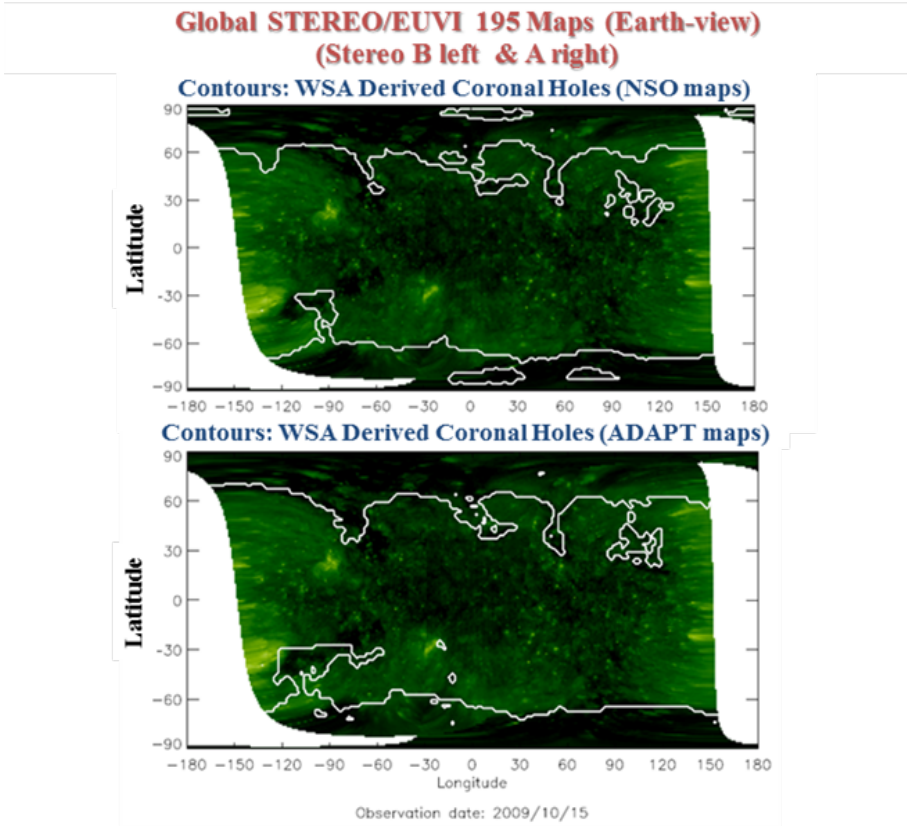


**Figure 10. STEREO A & B EUVI observations (green images) compared with WSA coronal hole predictions (white contours) using SOLIS (top) & ADAPT (bottom) maps as input to the model.**

Figure 10 is a comparison of WSA predicted coronal holes (white contours) and the global STEREO EUVI 195 observations (green images) of coronal holes (dark green regions). The plot on top are results obtained from WSA using traditional NSO/SOLIS maps to drive it, while the plot on the bottom is that obtained when using ADAPT maps. Note the improved agreement (e.g., left sides & poles of maps) between observations and the model when the ADAPT maps are used (bottom) compared that obtained using a traditional synoptic map (top). These results are what one would expect, since in traditional synoptic maps, the magnetic field observations on the Eastern hemisphere of the sun are normally the oldest and the polar fields regions are where

the observations are the least reliable. ADAPT helps to minimize both of these problems by both evolving the fields and using rigorous data assimilation.

## 4.4 Year 4

The research effort in year three focused on two main areas:

1. Improvement of the Los Alamos National Laboratory (LANL) Data Assimilation routine within ADAPT.
2. Testing and application of ADAPT.

### 4.4.1 LANL Data Assimilation Routine

Data assimilation of global solar magnetic fields presents a number of challenges. For instance, photospheric fields tend to form similar bipole patterns on various spatial scales. An ensemble data assimilation method such as the ensemble Kalman filter (EnKF) developed by LANL and used in ADAPT can produce unphysical bipole patterns in the northern and southern hemisphere of the sun, if not applied properly. This is exactly what happened in the initial implementation of the LANL Kalman filter. These unphysical patterns are a result of artificial correlations between the equatorial and polar regions of the Sun within the ensemble data assimilation. If left unchecked, the spurious correlations have the effect of introducing unphysical and unrealistic noise in the final model. An example of this is shown in the left image of Figure 11.

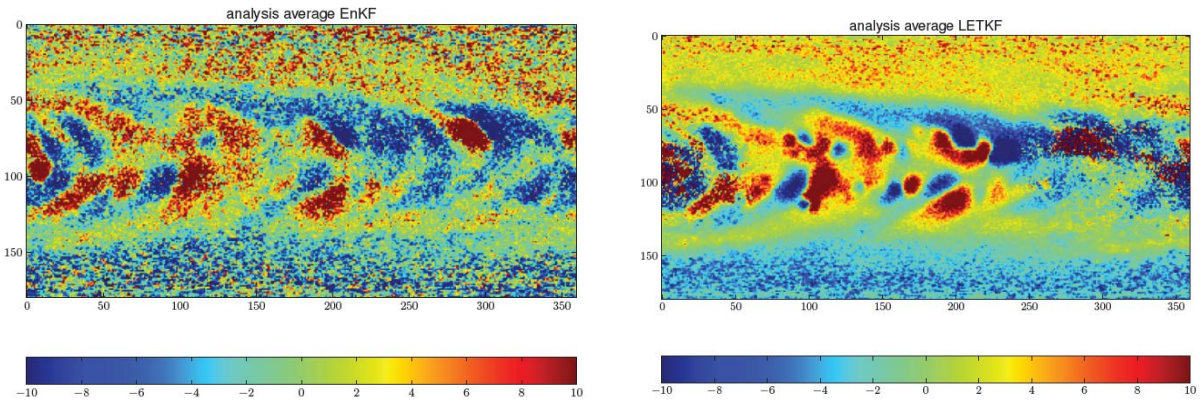


**Figure 11.** Sample ADAPT map with the standard EnKF implementation (left image). The effects of the spurious correlation are clearly visible (particularly at the poles) in the small spatial scale mixed polarity noise. The right image is an ADAPT map using the new LETKF implementation.

In order to suppress these artificial correlations, a local ensemble transform Kalman filter (LETKF) for the assimilation of data within ADAPT was implemented. The LETKF is a localized version of the EnKF where each gridpoint of the spatial domain is updated with local observations that lie in a local domain of interest. This domain is defined by the dynamics of the model to reflect the neighboring gridpoints that have an influence on the gridpoint. Each observation may be used more than once, depending on the size of the local domain for each gridpoint. This results in a smooth solution across the spatial domain of the problem. The main

advantage of the LETKF is that it eliminates all long-range spurious correlations and delivers a clean solution that is free of noise. Additionally, the algorithm is highly parallel since all gridpoints can be assimilated simultaneously.

The left image of Figure 11 reveals unphysical polarization patterns near the poles produced by a noisy analysis in the standard ENKF assimilation methodology. This noise is caused by spurious correlations in the model covariance matrix. On the other hand, the right image of Figure 11 shows a clean LETKF solution where the unphysical polarization near the poles is no longer present. Additionally, the spatial region where recently observed data was available includes far less spurious noise.

#### 4.4.2 WSA Solar Wind Model Comparison with STEREO B Observations

Solar wind speed and interplanetary magnetic field (IMF) polarity predictions model using traditional daily updated maps from NSO/SOLIS and ADAPT maps as its input were compared with in situ STEREO B observations. The comparisons were made using magnetograms from Carrington Rotation 2089 corresponding to mid-October to mid-November 2009. During this time the Sun was very quiet and the current sheet was very flat. In this particular configuration the ambient solar wind can be very difficult to predict, since the sub-satellite positions in the ecliptic plane run parallel to steep gradients in the solar wind speed and IMF (i.e., small uncertainties in the latitudinal positions of coronal structures produced by the model can result in large differences in the model predictions). This is one reason why this period was selected for testing (i.e., because of the difficultly to accurately model) along with the fact that the corona is slowly evolving at this time.

It was found that the WSA solar wind speed and IMF polarity predictions using the ADAPT maps as input to the model consistently outperformed the predictions obtained using traditional daily updated maps from NSO/SOLIS. One must keep in mind that the same magnetograms were used to produce both the ADAPT and NSO/SOLIS input maps. The difference being is that ADAPT assimilated the magnetograms using rigorous data assimilation methods along with evolving the magnetic fields using the WH flux transport model over time, while NSO/SOLIS maps were assembled using traditional but simplistic methods (see [29] for details). Figure 12 shows a comparison of the WSA solar wind speed predictions versus STEREO B in situ observations using traditional NSO/SOLIS maps (Top Left) and ADAPT maps (Bottom Left) as input to the model. Overall the match is better for the results using ADAPT as its input. The same is true for the IMF polarity predictions (Left Panels) where we see that the ADAPT results do a bit better than those from NSO/SOLIS. What is noteworthy here is that the WSA solar wind predictions for STEREO B come from the photospheric region on the Sun where the input data are the oldest and thus the flux transport process in ADAPT played the largest role. This suggests that ADAPT generates maps of the photospheric field that really do represent a more realistic snapshot of its global state at any given time.

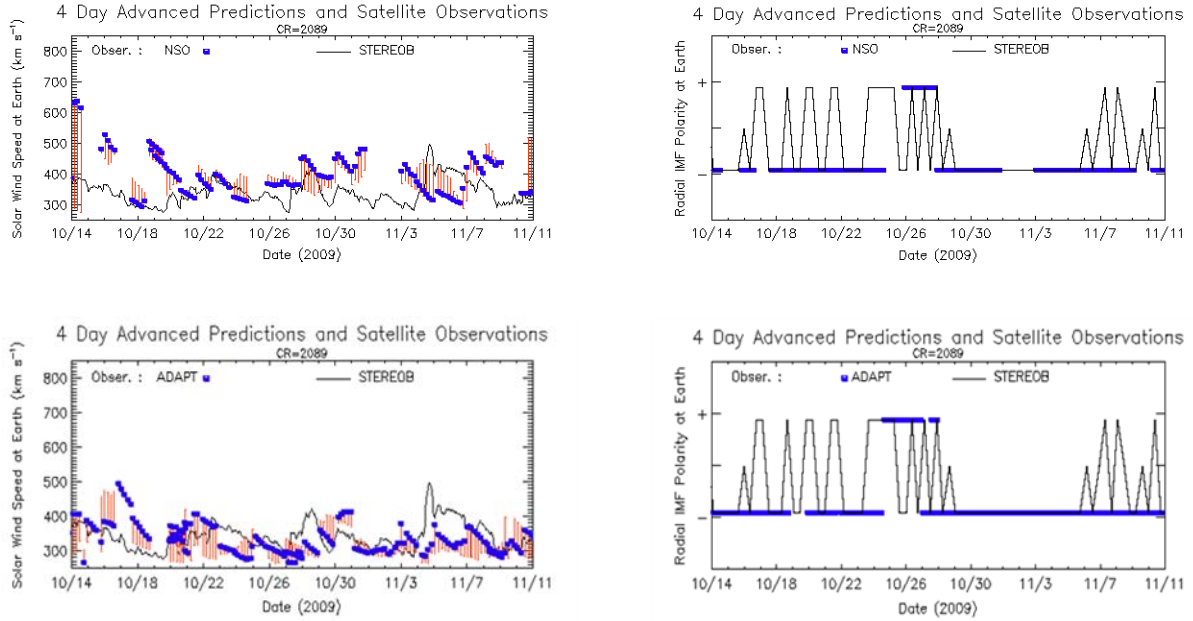


**Figure 12.** (Left) Solar wind speed predictions (blue dots) generated by WSA at STEREO B using traditional NSO/SOLIS (Top) and ADAPT (Bottom) maps compared to in situ observations from STEREO B (black solid cell). (Right) WSA IMF polarity predictions (blue dots) vs. observed (black solid line) polarity at STEREO B.

## 4.5 Year 5

The research effort in year five focused on two main areas:

1. Continued improvement of the ADAPT model and modifying it so that it can assimilate far-side active region observations.
2. Testing ADAPT maps in corona and solar wind models and using them in the development of a new, more reliable method for forecasting solar 10.7 cm (2.8 GHz) radio flux.

### 4.5.1 ADAPT Development

Year five's effort focused heavily on modifying ADAPT so that it could assimilate far-side detections of large active regions into the model. This required putting the helioseismic data in a form that ADAPT could readily use and then modifying the code so that it could ingest and assimilate these data. The other major focus for improving the ADAPT model was parallelization of the LANL data assimilation routine.

#### 4.5.1.1 Detecting Far-Side Active Regions

The detection of large active regions on the far-side of the Sun is possible using the helioseismic acoustic holography technique (see, e.g., [13] and [14]). It is based on comparing, for each location on the solar surface, the travel path determined for observed waves (as velocity field perturbations in the solar photosphere) with that determined by a model of the quiet Sun. When

waves travel through an area of concentrated magnetic field, they accelerate producing a phase shift with respect to the model. The phase shift is then calibrated in terms of magnetic field strength following [15] and a probability of detection is assigned to each active region identified using the results from [30]. The method is used to construct maps of active regions on the non-visible hemisphere of the Sun both from GONG and HMI Dopplergrams in a near-real-time fashion (see <http://farside.nso.edu>).

To begin using the helioseismic maps of active regions as input to ADAPT, the far-side maps had to be modified in the following manner:

1. Change the projection grid to Longitude-Latitude
2. Change the 2D file containing a map to a 3D file which includes the following three planes:
  - a) Magnetic field strength plane
  - b) Probability plane
  - c) Associated error plane

The errors were calculated from the dispersion relation found in [15]. However, work was pursued to improve on this approach by factoring in the data coverage and positions of the data gaps in the error calculation.

Additional developments opened the possibility of increasing the signal-to-noise in the helioseismic far-side maps. Preliminary analysis showed that the detection of active regions of medium size benefits from the addition of the correlation between the signals of the waves traveling a path that bounce once at the solar surface (2skip) with those that bounce twice (3skip). In year five (2012), the maps were constructed by combining near-side observations of waves that have bounced once at the solar surface (i.e., 2x2skip), which allow the central portion

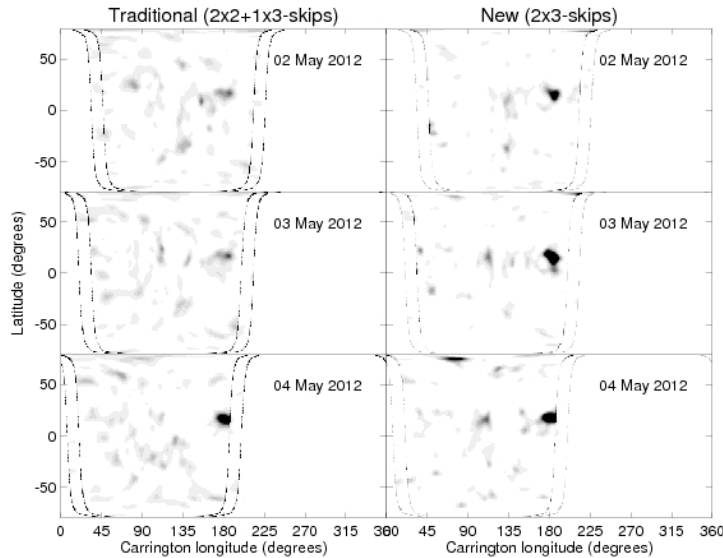


**Figure 13. Comparison between calibrated far-side seismic maps built using the traditional combination of 2x2skip and 1x3skip (left) with the newly calculated 2x3skip (right). The sequence spans May 2 to 4 2012 and shows the signature of active region NOAA 11476 on the far-side three days leading to its appearance on the front side at the East limb. The dashed lines indicate the non-visible hemisphere of the Sun. There are double lines in each map because we average 2 consecutive days to improve the signal-to-noise in the calculations.**

of the far-side disk to be imaged, with those having no (1skip) and two (3skip) surface bounces (i.e., 1x3skip), which allow the limbs of the far-side disk to be imaged. Calculations showed that including the correlation of the signal of the 2skip with that of 3skip paths for a 2x3skip over the whole far-side surface enhances the signal-to-noise of the maps (see Figure 13) thus making detection of far-side active regions more reliable.

#### 4.5.1.2 Incorporating Far-Side Data into ADAPT

The ADAPT model code was been modified to assimilate the far-side active region data described in Section 1.1 above. Since the helioseismic inference of the field strength on the far-side does not discern polarity information, known statistical and cycle properties for active regions are utilized (i.e., Hale's and Joy's rules) to estimate the polarity order and orientation. As a preliminary test to estimate the polarity distribution of the far-side active region, the field strength signal was split east-west (shown in Figure 14), to nearest equal sums, making one half negative (depending on hemisphere and current cycle), then scaled so that the mean flux of the active region sums to zero. When merged with the ADAPT map, the mean of the replaced pixels is preserved to avoid introducing a monopole to the global map.

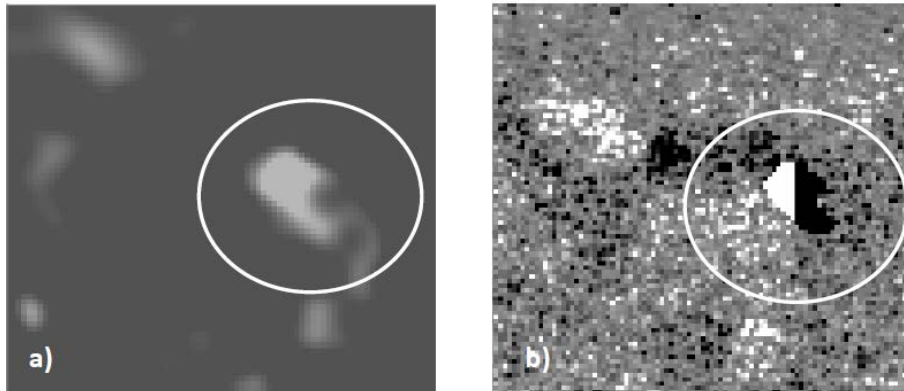


**Figure 14. Example of the initial “basic” polarity estimation method. An input far-side signal (shown in a and highlighted by the white ellipse), from 1 Jul. 2012, is split in half (with a scaling correction to remove residual polarity imbalance) with the selected polarities dictated by Hale’s law and the current cycle (shown in b).**

Expanding from the preliminary test shown in Figure 14, work started on a method to translate the far-side signal into a more realistic flux distribution and polarity. The polarity estimation method developed transmogrifies the “basic” polarity distribution around split centroids (dependent on the far-side signal & area) tilted relative to Joy’s law for the given latitude (see Figures 15 and 16).

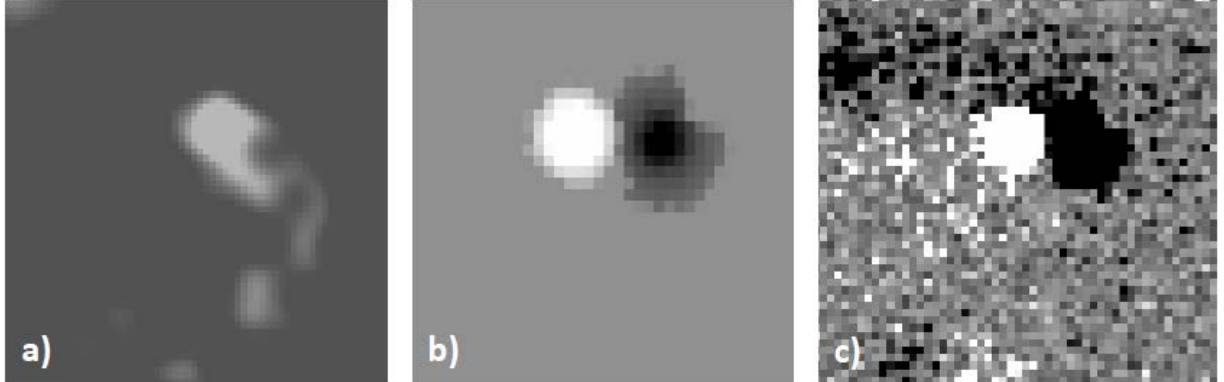


**Figure 15.** Example of the new polarity estimation, which transmogrifies the “basic” polarity distribution around split centroids (dependent on the far-side signal & area) tilted relative to Joy’s law for the given latitude.

Figure 16 displays a far-side merging, showing the evolution within the ADAPT map, where the far-side signal is merged on July 1, 2010 (upper left) using the new method. The Earth-side observation of the active region begins to be assimilated on the 8<sup>th</sup> through the 10<sup>th</sup>. The final frame (07/12) is nearly 100% observation, whereas the July 7<sup>th</sup> image is 100% far-side flux and polarity estimation with ADAPT.

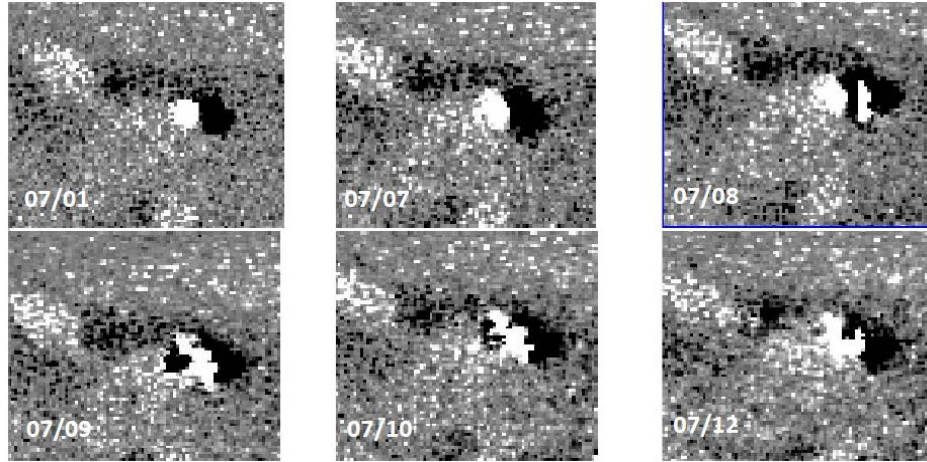


**Figure 16.** Far-side merging example reveals the evolution within the ADAPT map, where the far-side signal is merged on July 1, 2010 (upper left) using the new method. The Earth-side observation of the active region begins to be assimilated on the 8<sup>th</sup> through the 10<sup>th</sup>. The final frame (7/12) is nearly 100% observation, whereas the July 7<sup>th</sup> image is 100% far-side flux and polarity estimation with ADAPT.

#### 4.5.1.3 Parallelization of the LANL Data Assimilation Routine

The ADAPT model was modified to use the local ensemble transform Kalman filter (LETKF) [22] methodology for data assimilation. The LETKF assimilates each model grid-point, defining a local area of interest and determining which observations are included within this area (see Figure 17). The main advantage of LETKF is that all grid-points can be assimilated simultaneously using parallel computation. The parallelization of the assimilation was

implemented using the Message Passing Interface (MPI) framework within Fortran 90. The method implemented assigns the assimilation of a batch of model grid-points to each CPU, along with the grid-points and observations that fall within the local area of interest. Once the assimilation is performed, the appropriate model grid-points are updated and the complete grid is assembled from all CPU's. The parallel algorithm was tested in a two-dimensional shallow water model with encouraging results in performance. Once the ADAPT model has complete parallel capabilities (i.e., each model realization can be run in parallel), the plan was to incorporate the parallel version of the assimilation into the ADAPT code.

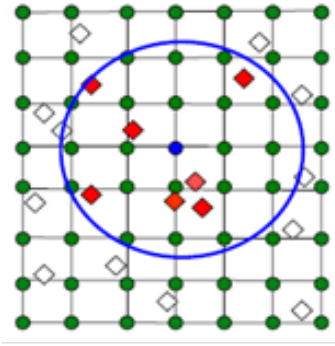


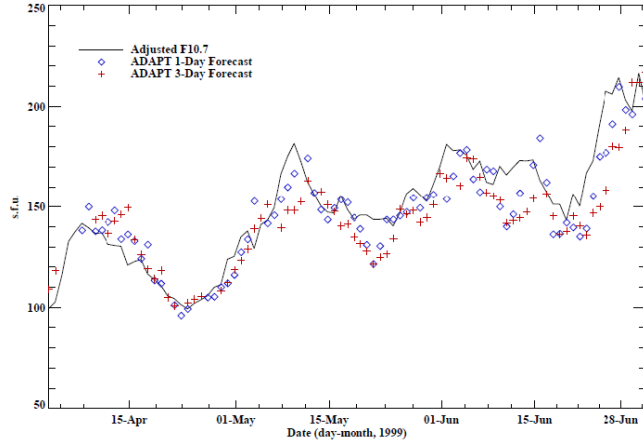
**Figure 17.** The LETKF algorithm assimilates one model grid-point at a time (blue dot) by defining a local area of interest (blue circle) and identifying any observations that fall within the local region (red diamonds).

#### 4.5.2 Testing and Application of ADAPT

ADAPT maps with and without the far-side data included in them were tested in models of corona and solar wind. They were also used in the development of a new and unique method for forecasting the solar 10.7 cm (2.8 GHz) radio flux [31]. This latter work spurred a new research effort within the group to better understand the physical relationship between solar magnetic fields and 10.7cm radio flux.

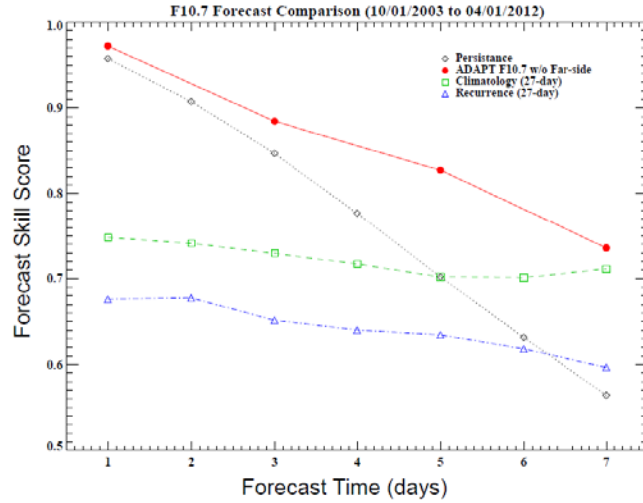
##### 4.5.2.1 Forecasting F10.7 with ADAPT

As an example of a direct application of ADAPT to space weather prediction, a new method was developed to forecast the solar 10.7 cm (2.8 GHz) radio flux, abbreviated F10.7, utilizing advanced predictions of the global solar magnetic field generated by ADAPT. Using indices derived from the absolute value of the solar magnetic field, a good correlation was found between the observed photospheric magnetic activity and the observed F10.7 values (e.g., see Figure 18). Comparing magnetogram data observed within six hours of the F10.7 measurements during the years 1993 through 2010, the Spearman correlation coefficient,  $r_s$ , for an empirical model of F10.7 was found to be 0.98. In addition, little change in the empirical model coefficients and correlations between the first and second 9 year intervals of the 18 year period investigated was found. By evolving solar magnetic synoptic maps forward 1-7 days, this new method provides a realistic estimation of the Earth-side solar magnetic field distribution used to forecast F10.7. Spearman correlation values of approximately 0.97, 0.95, and 0.93 were found for 1 day, 3 day, and 7 day forecasts, respectively. This unique method was eventually expanded to forecast other space weather parameters, e.g., extreme ultraviolet flux.



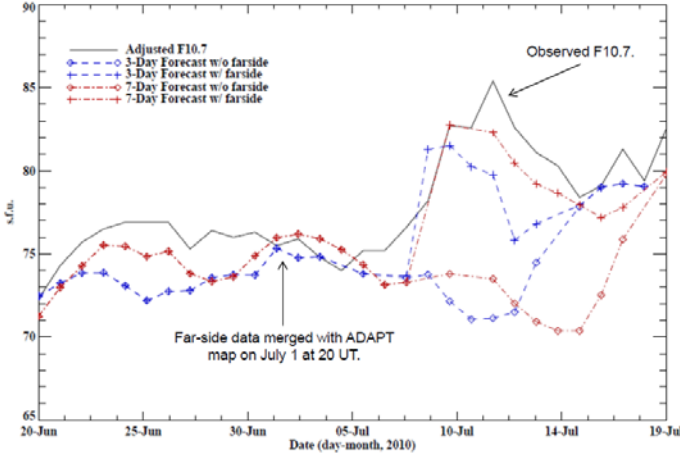
**Figure 18. Three month comparison between the 1-day (diamond) & 3-day (+) forecast values from ADAPT global magnetic maps and the observed F10.7 (solid line), shown for April through June 1999.**

Figure 19 shows a comparison between the ADAPT F10.7 empirical model and standard forecasting models (persistence, climatology, and recurrence), displaying the forecast skill score relative to forecast time in days. Though the empirical model is clearly best, without far-side data, all space weather forecasting models are driven by and reliant on the persistence and recurrence of past observations.



**Figure 19. Skill score comparison between the ADAPT F10.7 empirical model (red dots) and standard forecasting models: persistence (diamond), climatology (boxes), and recurrence (triangles).**

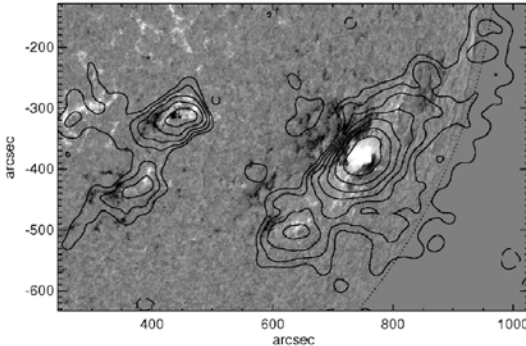
As a check of the estimated field strength and location, the merged and evolved far-side signal within ADAPT maps (i.e., discussed in Section 4.5.1.2) were also used to model F10.7. The inclusion of the far-side signal, illustrated in Figure 20, resulted in predicted values in excellent agreement with the observed radio flux, providing preliminary validation of the calibration of the original far-side area, location, and field strength values.



**Figure 20.** Comparison between ADAPT modeled F10.7 forecasts with (plus signs) and without (diamonds) including far-side data and the observed F10.7 values, clearly showing that the inclusion of the far-side signal improves the agreement.

#### 4.5.2.2 Sources and Physics of F10.7

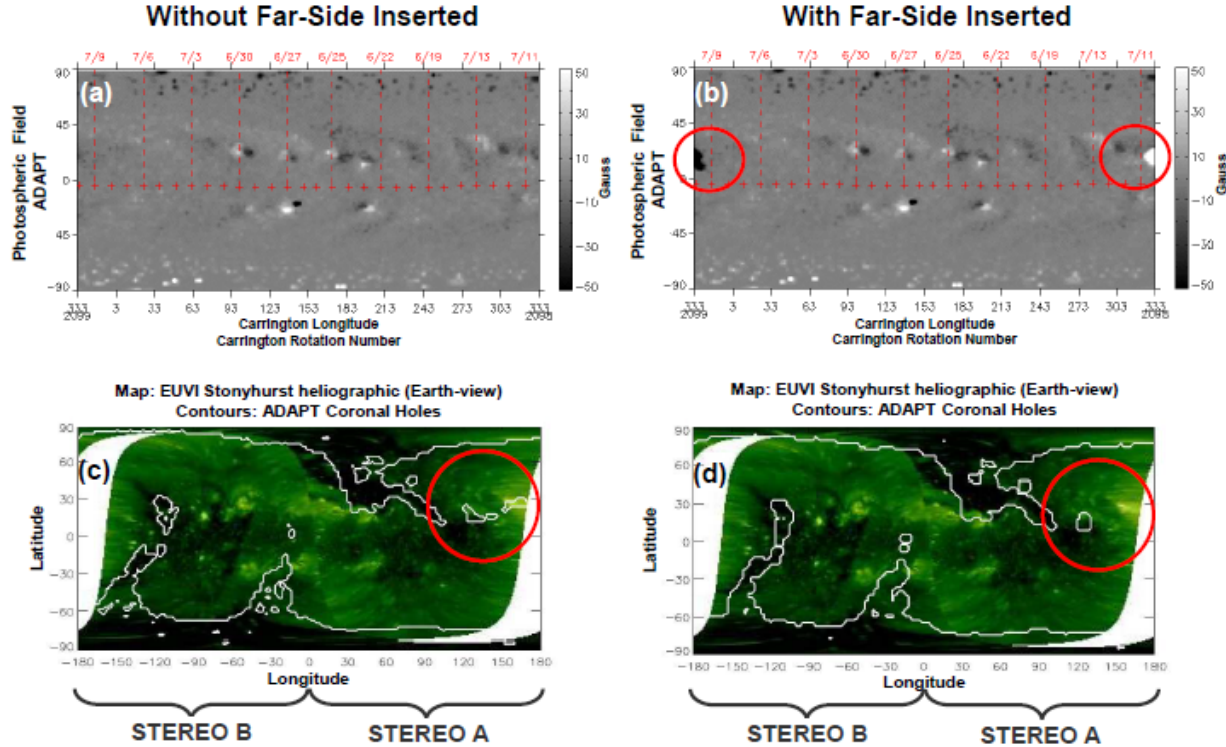
A better understanding of the sources of the solar 10.7 cm radio flux signal was critical to improving the empirical model development and evolving to a model atmospheric solution. For instance, a more detailed understanding of the F10.7 source locations in relation to the photospheric magnetic field was expected to be achieved by directly comparing the two. Progress in this direction was made in year five through the construction of the first ever, partial disk, comparison (Figure 21) of F10.7 observations from the EVLA (Expanded Very Large Array) with SDO/HMI magnetogram data. Comparison work between EVLA and magnetogram image data is anticipated to aid in the determination of the minimum spatial resolution for the global magnetic maps needed to improve future F10.7 forecast models. In addition, the observational study is expected to provide feedback on the limitations of the simple empirical model outlined in the Section 4.5.2.1. The benefit of using ADAPT global solar magnetic maps is that one can move away from an empirical model toward a physics-based model for forecasting F10.7 9e.g., [32]). Ultimately, daily spatially resolved F10.7 observations (see [33]), would permit long-term feedback and refinement of flux transport models like ADAPT.



**Figure 21.** Preliminary reduction of 1 of the 7 fields that comprise the solar full-disk obs at 2.8 GHz (10.7 cm; intensity contours) from the EVLA, observed on Dec 9, 2011, shown with a corresponding HMI magnetogram (grayscale image).

### 4.5.2.3 WSA Coronal & Solar Wind Predictions With & Without Far-Side Detected Active Regions Included

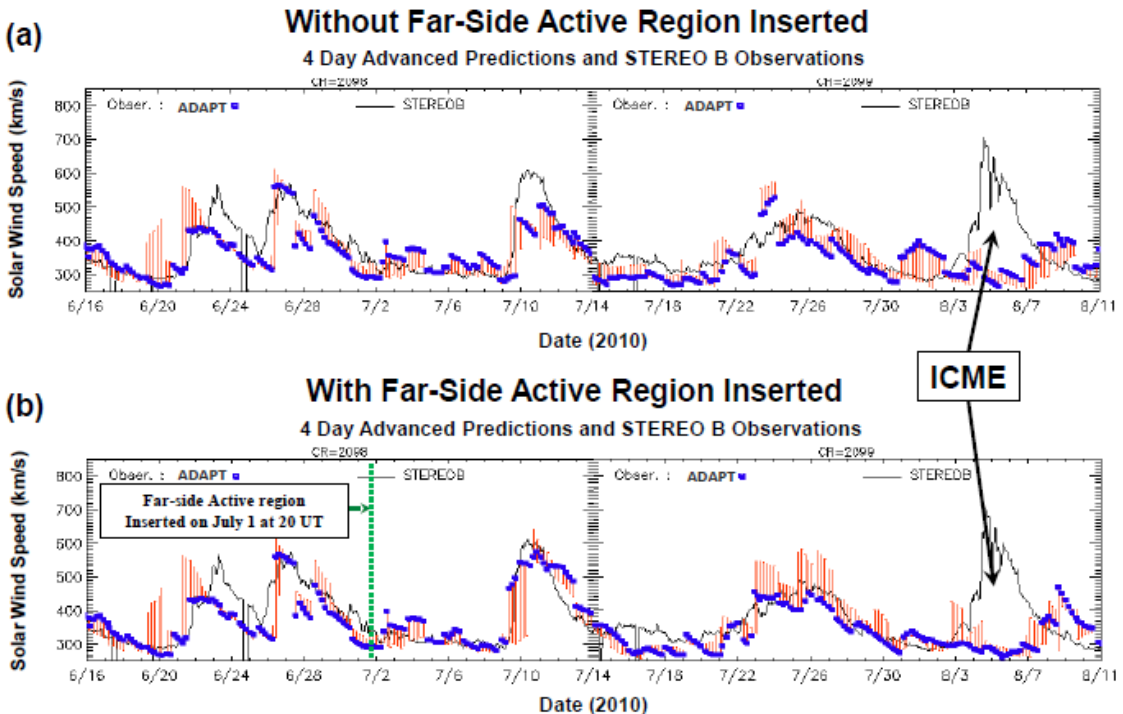
As a preliminary evaluation of the far-side assimilated ADAPT maps developed in year five, they were tested in the WSA coronal and solar wind model [34]. Specifically, coronal Extreme Ultraviolet (EUV) and in situ solar wind observations available from STEREO were compared with WSA model predictions when it was driven by ADAPT maps with and without the far-side active region (AR11087) included in them (see Section 4.5.1.2). Two sets of daily photospheric magnetic field maps spanning two solar rotations were thus generated using the ADAPT model. The first set includes the far-side observation of the active region, while the second is without the far-side data. Figure 22 illustrates two ADAPT photospheric magnetic field maps (a & b) from July 1, 2010, the day the far-side active region data was merged. Figure 22a exhibits the original ADAPT map without far-side data, while Figure 22b shows the ADAPT map with the far-side active region included. The red crosses in both figures correspond to the sub-STEREO B positions.



**Figure 22.** ADAPT photospheric magnetic field without far-side active region included (a) and with the far-side active region included (b) shown in upper row. The comparison of global STEREO EUVI map (green image) and WSA coronal hole predictions (white contours) rendered in (c) & (d) were obtained using (a) & (b), respectively, as inputs to the WSA model. Note that the small coronal hole positioned on top of the bright area of EUV emission (circled in red) in (c) has disappeared in (d).

The same global STEREO EUVI map (i.e., the green images) corresponding to July 1, 2010 is shown in both Figures 22c & 22d. The map was constructed from the individual STEREO A & B EUVI disk images from that particular day. The global EUVI maps are co-aligned with the photospheric field maps displayed in Figures 22a and 22b, except that the longitudes displayed

on the horizontal axes of these figures indicate distance from the central meridian (i.e., longitude  $153^{\circ}$  in Carrington coordinates) with east/westward being negative/positive. Overplotted on these two EUVI maps are white contours depicting WSA coronal holes predictions based on using the two ADAPT maps seen in Figures 22a & 22b as input to the model. The agreement between the observed coronal holes (primarily the dark regions in the EUVI map) and that determined by WSA is reasonably good. An area of interest, circled in red in Figure 22c, is where three small coronal holes are predicted. In particular, the rightward-most coronal hole within the circle is positioned right on top of a small area with very bright EUV emission. This bright region is associated with the negative polarity of the active region located at  $\sim 305^{\circ}$  longitude and  $\sim 25^{\circ}$  latitude. This small hole is almost certainly not real, as coronal holes are usually dark in EUV, and it is not predicted by WSA when the large far-side active region is included in the ADAPT model (as illustrated in Figure 22d).



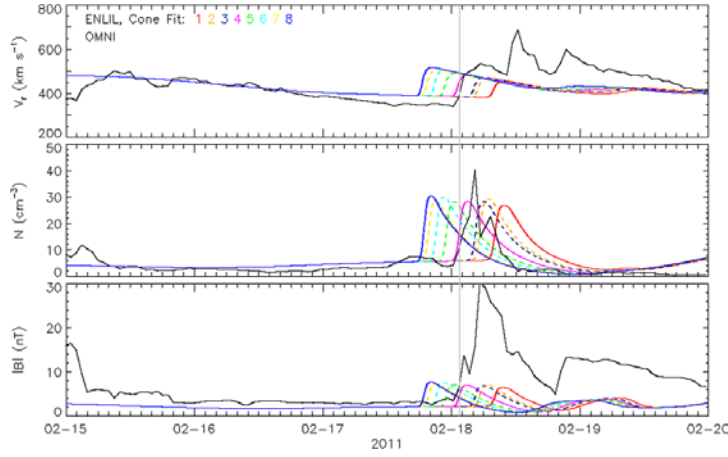
**Figure 23.** Solar wind speed observations from STEREO B (black solid lines) vs. WSA predictions (blue dots) using daily ADAPT maps without the far-side active region included (a). The lower time series (b) is the same as (a) except now using ADAPT maps with the far-side active region included. The red vertical bars indicate the range over which WSA solar wind speed predictions vary over a grid cell.

Figure 23 features a comparison between the WSA predicted solar wind speed (blue dots) at the position of STEREO B and the in situ observations (solid black line) from that spacecraft over the time interval CR2098-2099. Figure 23a compares model predictions and STEREO B observations when the far-side active region is not included in the ADAPT maps, while Figure 23b demonstrates the comparison when it is included. In both cases the agreement between model predictions and observations is quite good. The only major discrepancy found is for the interplanetary coronal mass ejection (ICME) that arrived at STEREO B on August 4, 2010. Since WSA only predicts the slowing varying background solar wind, it is not expected to capture ICMEs. Comparing the results highlighted in Figures 23a & 23b, note that the predictions in both are identical to each other until about July 6, 2010. This is true even though the far-side active

region was assimilated into the ADAPT maps on July 1. This makes sense physically because it takes slow solar wind traveling at  $\sim 300$  km/s about 5 days to reach 1AU. After July 6, the two solar wind prediction time series begin to differ noticeably from each other with those that include the far-side active region having better overall agreement with observations, especially for the high speed stream recorded by STEREO B on July 10.

#### 4.5.2.4 Ensemble Modeling of CME Propagation Using ADAPT

In a study to determine the sensitivity of WSA+Enlil model predictions of CME arrival times to the initial input of the CME geometry [35], an ensemble of numerical simulations was created by varying the CME parameters used to initialize the Feb. 15, 2011 halo event in the model. It was found that the accuracy of the WSA+Enlil modeled arrival times not only depends on the initial input CME geometry, but also on the accuracy of the modeled background solar wind, which is driven by maps of the photospheric field. In effort to improve the modeling of the background solar wind, ADAPT maps were used as a driver to the model. An advantage of the ADAPT maps is that they provide a more instantaneous snapshot of the global photospheric field distribution than that provided by traditional daily updated synoptic maps. When a traditional synoptic map was used as the driver to the WSA+Enlil+cone model, the spread in the ensemble set of eight different CME arrival time predictions was found to be about  $\sim 13$  hours with the ensemble average arriving about 9.5 hours earlier than observed. When an ADAPT map was used to drive the background solar wind, the spread in CME arrival times remained about the same as before but now had an ensemble average that was nearly centered on the observed CME shock arrival time. In the top panel of Figure 24, the modeled radial speeds (colored lines) at 1 AU using the ADAPT input map provide a much better match with the *in situ* values (solid black line), particularly during the days leading up to the arrival of the CME disturbance. By using a more accurate model background solar wind through which the cone CME propagates, the resulting set of arrival time predictions match the observations much better.



**Figure 24.** Time series of the near-ecliptic solar wind parameters at 1 AU for (top) radial speed, (middle) density, and (bottom) magnetic field magnitude. The colored lines are the simulation results from WSA-Enlil, where each color represents the simulation result for each cone fit from our ensemble for the 15 February 2011 CME. The *in situ* L1 observations from the OMNI data set are shown in solid black. The gray vertical line marks the approximate (observed) shock arrival time of the CME at Earth.

## 4.6 Year 6

The research effort in year six focused on three main areas:

1. Further improvement of the ADAPT model:
  - a) Parallelization of the code.
  - b) Improved handling of the flux transport process at the poles.
  - c) New method to remove the data assimilative residual (“monopole”) signal.
  - d) Improvement in the data assimilative methodology and efficiency.
2. Continued to improve the far-side input data for the ADAPT model:
  - a) Improved the reliability of the far-side active region detections and phase signal-field strength calibration.
  - b) Improved the methodology for assimilating far-side data into ADAPT.
  - c) Developed methods for specifying the polarity order and distribution and the tilt of the active region detections.
3. Application of ADAPT maps:
  - a) Developed a brand new and unique method for forecasting solar EUV/XUV/FUV using ADAPT maps.
  - b) Modified the WSA coronal and solar wind model so that it could readily incorporate ADAPT maps into it.

### 4.6.1 ADAPT Development

Several key enhancements occurred during year six to the ADAPT model software that helped speed up the development-test cycle, improved the modeling of the magnetic flux transport in the polar regions, removed the data assimilative residual (“monopole”) signal, increased collaborative feedback, and improved the data assimilative methodology and efficiency used in the model.

#### 4.6.1.1 ADAPT Parallelization

Early in the year, the parallelization of the forward modeling functions, so individual realizations can be processed simultaneously, resulted in a processing speedup of four times compared to the previous version. This improvement allowed for multiple 10-year study runs during a typical day for rapid development testing and fine-tuning model parameters. The faster modification-test cycle time allowed, for example, a detailed comparison between VSM (~1 day cadence) and GONG (~1 hr cadence) input data. The two instrument comparison led to a better understanding of a previous finding with the VSM input data that required asymmetric meridional flow rate between the hemispheres, to match polar observations. With the addition of GONG data, it is clear that the VSM signal quality varies from south to north (source still unknown, could be instrumental focus or flat changes during observation) that results in an artificial polar hemispheric asymmetry in polar field strength. An example of the ADAPT polar field prediction values using GONG is shown in Figure 25.

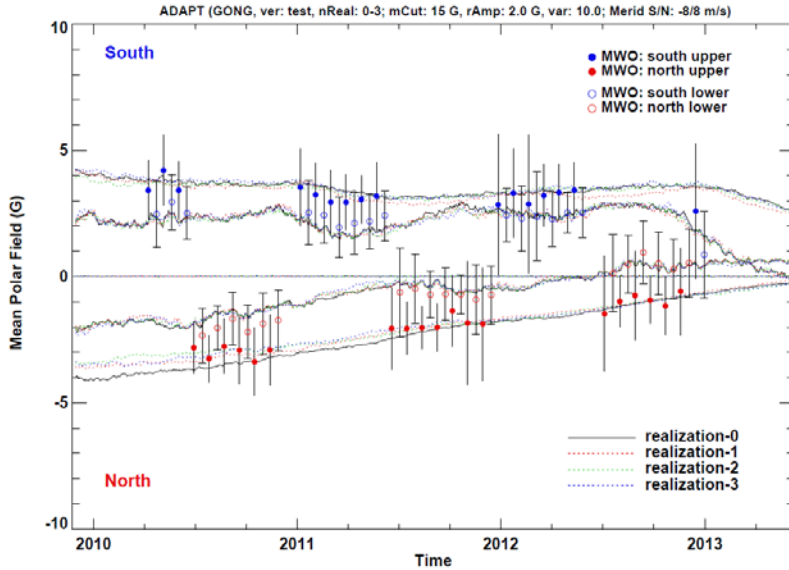


**Figure 25.** Modeled polar mean values compared to observation, using NSO/GONG magnetograms as input. The open circle (lower: 62-70 degrees latitude) and closed circle (upper: 70-90 degrees latitude) values are from the 150-ft solar tower at Mount Wilson Observatory (MWO). Also note that the four realizations shown are for identical model parameters, highlighting the nominal variation due to super granulation.

#### 4.6.1.2 New Monopole Removal Methodology

Another significant improvement made to the ADAPT model software in year six was the development and inclusion of a dynamic monopole removal algorithm. The residual monopole signals are typically generated from poorly observed solar limb data during the data assimilative process, especially for partially observed & assimilated flux from active regions. The typical solution employed by modelers is to simply subtract the residual signal from all pixels equally, which at times can be rather large (see the period delineated by the ellipse in Figure 26, illustrating deviations greater than 0.5 G globally). Since the main source of global map monopole signals is known to come from active regions on or near the observed limb, a method was developed to remove the monopole by rescaling active region fluxes with higher weights for regions near the recently observed limb. An example of partially dampening the monopole signal at assimilation is depicted by the ellipse period in Figure 27.

#### 4.6.1.3 Increased Collaborative Feedback

To expedite and improve interaction with outside collaborators, the ADAPT filenames and header metadata were upgraded to be more readily accessible with documentation for external users, e.g., NOAA and Predictive Science Inc. (PSI) collaborators. The new file format and metadata of the ADAPT maps allowed for improved collaboration, which resulted in constructive feedback on properties of the ADAPT model. For example, partners at PSI used ADAPT maps for detailed MHD heating in the polar regions and provided useful feedback regarding the modeled magnetic spatial scale of flux near the pole. This is an artifact of the reference frame (i.e., latitude and longitude) used to model the global flows that increases the spatial resolution at higher latitudes. To preserve the observed spatial scale, an adaptive smoothing of the flux at higher latitudes was implemented.

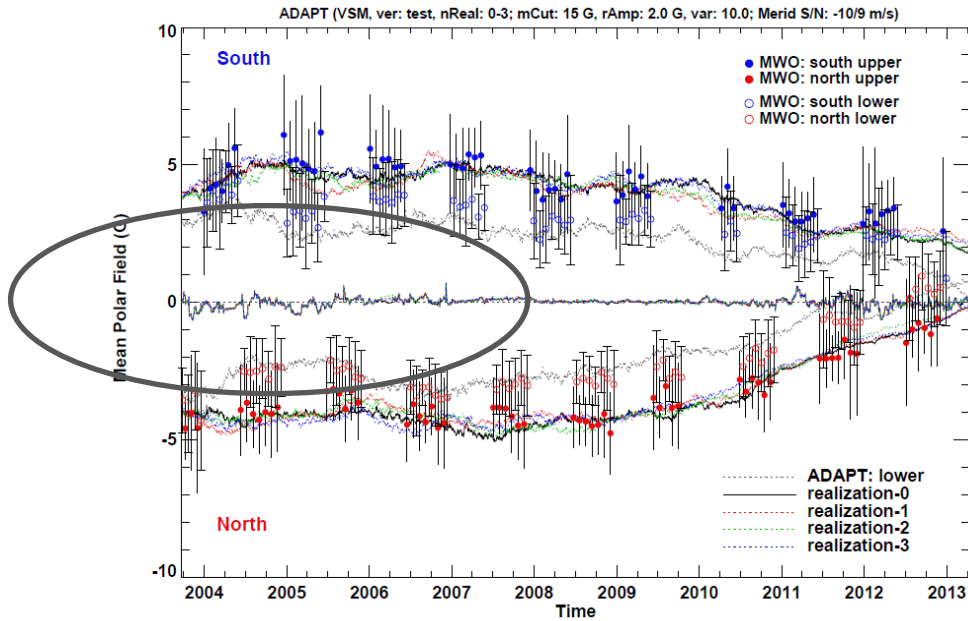


**Figure 26. Modeled polar mean values compared with observation.** The upper north/south latitude bands provide direct feedback on the model parameters, where the initial seed map includes best estimates of the polar field strength then no additional data is added at the poles for all future time steps during the 9 years. Also note that the four realizations shown are for identical model parameters, highlighting the nominal variation due to super granulation. The open circle (lower: 62-70 degrees latitude) and closed (upper: 70-90 degrees latitude) values are from the 150-ft solar tower at Mount Wilson Observatory (MWO).

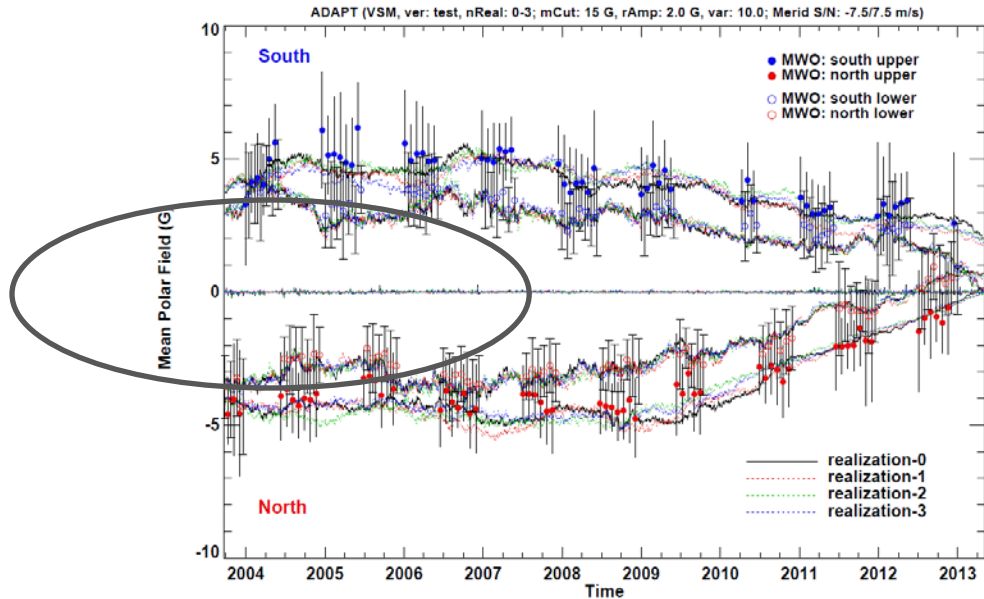


**Figure 27. Similar to Figure 26, but using a prototype monopole dampening method.** Comparing the period delineated by the ellipse with Figure 26, periods with large monopole signals have been partially dampened towards zero. In practice the dampening is set to 100% for final maps to be used as input to coronal models.

#### 4.6.1.4 LETKF Parallelization

A parallel version of the localized ensemble transform Kalman filter (LETKF) assimilation method [22] was successfully implemented in the ADAPT model. The parallel version of the LETKF takes advantage of the parallelization of the ADAPT code implemented by the AFRL team. Given that LETKF assimilates each model grid-point independently, the algorithm can be easily parallelized. Each grid-point is assimilated using a local region of the total domain that restricts the correlation of information so as to avoid the introduction of noise into the assimilation result. A local region is defined to be an ellipse elongated along the longitudinal direction of the global coordinates. The parallel program assigns the assimilation of a batch of model grid-points to each CPU, along with the grid-points and observations that fall within the local area of interest. Once the assimilation is performed, the appropriate model grid-points are updated and the complete grid is assembled from all CPU's.

In certain circumstances the LETKF can suffer from filter divergence, which is caused by the collapse of all ensemble members into the same state. This can be avoided by inflating the ensemble and restore a reasonable ensemble spread. In this way the assimilation can steer the ensemble towards the observations while correctly considering the uncertainty from both the model and observations. To avoid ensemble collapse an adaptive inflation technique [36] and [37] was implemented, which estimates an appropriate inflation factor on-line, as the assimilation is being performed. In this way the ensemble is inflated every time the assimilation is performed and prevents the collapse of the ensemble.

#### 4.6.2 The Helioseismic Far-side Data

Including solar far-side magnetic activity estimates is key to modeling more accurate forecast values and extending forecasts beyond 7 days. The detection of large active regions on the far-side of the Sun is possible using the helioseismic acoustic holography technique. Methods to improve the quality and reliability of far-side magnetic field data were further explored and tested in year 6. In addition, work was done to improve the methodology for assimilating into ADAPT far-side active region detections along with the specification of the tilt and polarity order and distribution of these regions.

##### 4.6.2.1 Far-Side Data Improvements

Far-side maps seem to gain signal when incorporating the 2x3skip schema into the calculations. However, for this calculation to be useful as input to ADAPT, it was realized that a full calibration in terms of the strength of the magnetic field needed to be done. The previous calibration that was in use in year six (2013) for the far-side helioseismic maps was performed by comparing the computed phase-shift of active regions at the non-visible hemisphere, with the photospheric magnetic field distribution that the same active regions exhibited when appearing on the front-side. Unfortunately, this approach assumes a non-evolution state for the active regions and is a crude approximation to reality. It was realized that the same approach could be used to calibrate the 2x3skip calculations. Figure 28 shows scatter plots relating the magnetic-field strength and the phase-shift obtained for the 2x2skip schema (left) and the 2x3skip new calculations (right) when using this approach. It is clearly seen that the same magnetic field

produces different phase-shift depending on the number of bounces associated with the waves that are included in the analysis.

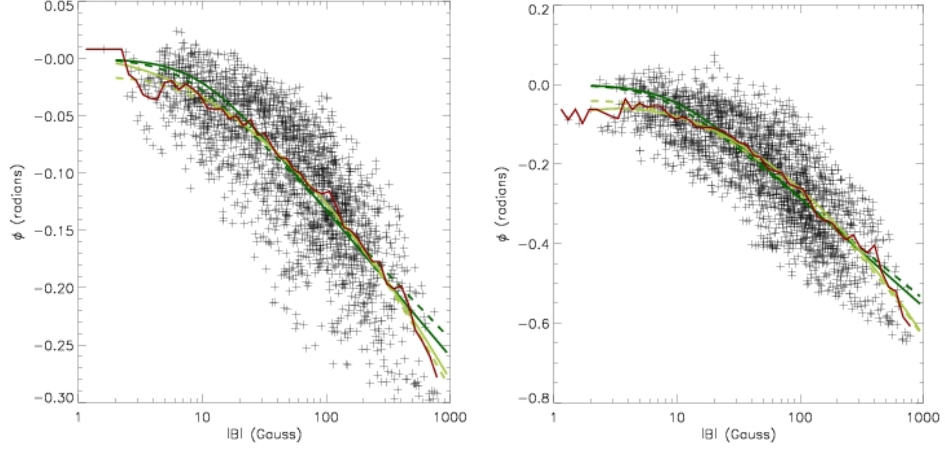


**Figure 28.** Scatter plot of the magnetic-field strength compared with the phase shift in helioseismic far-side maps associated to very large active regions. The right plot shows the results for the 2x2skip calculations and the left plot the ones associated to the 2x3skip schema. The different lines present the binned results (red) as well as the different fitted curves (green).

It was realized that a better way to calibrate the far-side maps could be achieved by using ADAPT maps, as the 4-day evolved photospheric magnetic maps calculated by ADAPT proved to be very accurate.

A plan was proposed to use far-side maps of large active regions that have rotated onto the far-side four days prior and to compare them to the magnetic flux distribution obtained by evolving the front-side magnetograms with the ADAPT code. This approach allows for simultaneous comparison of the phase-shift associated to the active regions in the helioseismic maps and the strength of the magnetic field.

Ultimately the goal for the far-side maps was to include the 2x2 and the 2x3skip calculations in a merged fashion so they like the preliminary one shown in Figure 29.

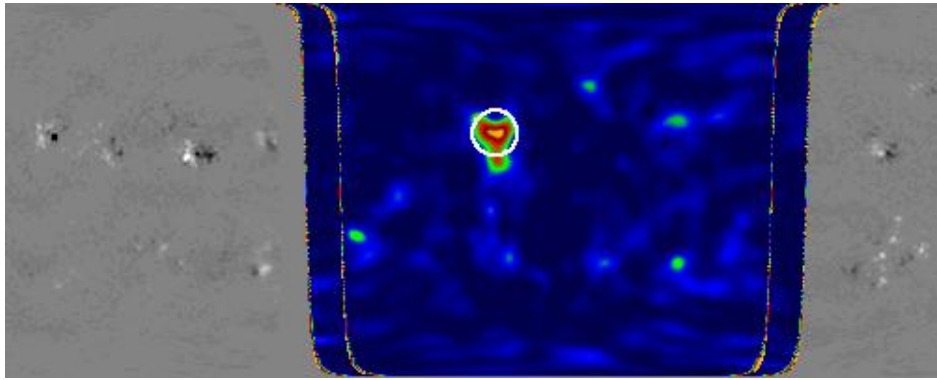


**Figure 29.** GONG far-side map calculated with an ad-hoc combination of a 2x2skip and a 2x3skip map for May 23 2012. It clearly shows an active region that rotated to the front side on May 30 2012. The formal calibration in term of magnetic-field strength is still a work in progress.

#### 4.6.2.2 Far-Side Active Region Specification and Assimilation

In year six, a new far-side ADAPT sequence was generated, for collaborative work with PSI, blending the new far-side flux emergence over 12 hours rather than an abrupt merger done previously. In addition, work was started by an NMSU summer space scholar to further improve magnetic modeling capabilities by selecting far-side active region morphologies from GONG data. Using near-side GONG and ADAPT synoptic maps, it was found that morphological features of the helioseismic phase signal can be used to better estimate the active region size, tilt angle, and polarity distribution. For this study [38], ADAPT maps were compared directly with GONG near-side maps for January 5, 2002-December 31, 2005, an example is shown in Figure 30.

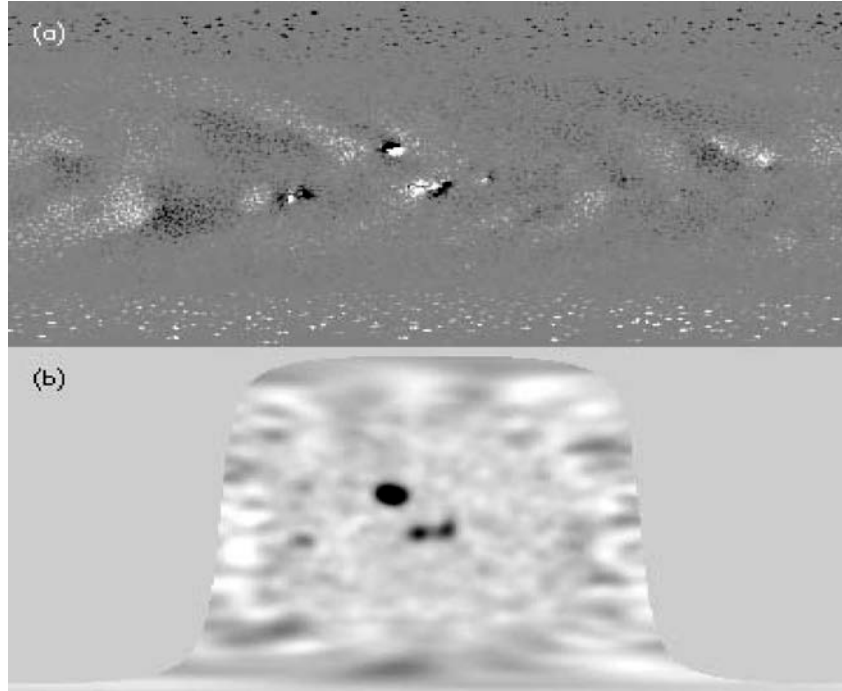


**Figure 30 - Example ADAPT.** (a) *synoptic map showing the global solar magnetic flux distribution. North & South magnetic polarities are seen in black & white, respectively. In addition, an example GONG near-side map (b) with far-side masked. Both panels are co-temporal. Three strong active regions can be seen in both maps.*

The study utilized various morphological parameters that were calculated once phase regions were found to be above a minimum size (based on a threshold found to relate to active regions). The parameters considered include: the phase barycenter; positive, negative, and unsigned magnetic polarity centroids; phase and magnetic polarity tilt. The areas of the phase and corresponding active regions are shown in Figure 31.

For this preliminary study, magnetic polarity tilt is estimated from the slope of the line connecting the two active region polarity centroids. Phase region tilts are taken from a least-squares ellipse fit to the loci of points of a particular region. No projection corrections are applied since both data are in the same spatial reference frame (i.e., latitude and longitude). Active region tilt is another morphological feature that was extracted from GONG near-side data. Magnetic polarity tilt is calculated from the line connecting the two polarity centroids in an

active region. The phase region tilt is taken from the tilt of an ellipse fit to the loci of points in a phase region. Shown in Figure 32 is the comparison between the magnetic and phase tilt. In general there is a good agreement between the two tilts.

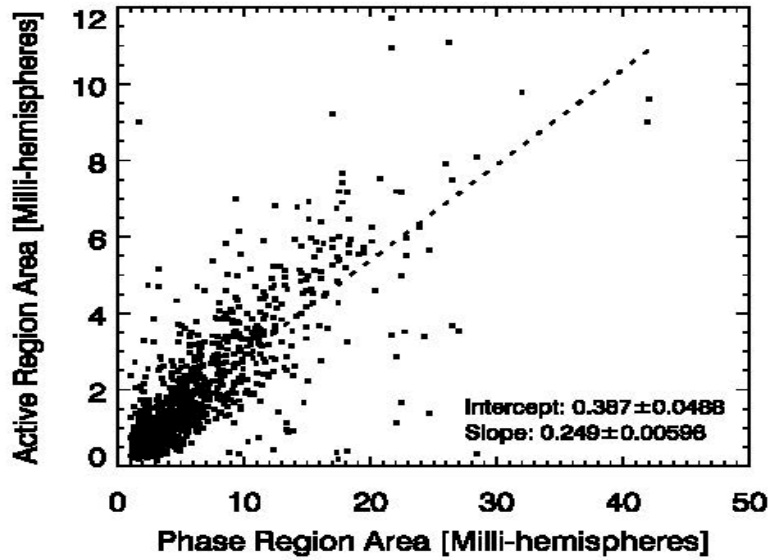


**Figure 31.** Comparison between the area of active regions and the areas of phase regions, where area is expressed in units of milli-hemispheres. Though the active region areas are dependent on the threshold chosen, once selected a linear relationship can be found to translate the helioseismic phase area into observed magnetic area.

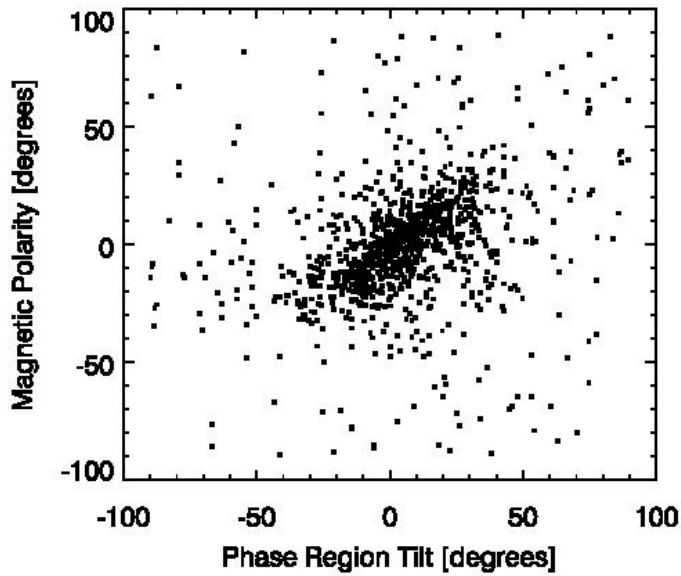


**Figure 32.** Magnetic polarity tilt plotted against phase region tilt. Polarity tilts are calculated from the slope of the line connecting the two polarity centroids. Phase region tilts are a result of an ellipse fit the active region.

These preliminary results indicated that it would be useful to pursue assimilating the helioseismic phase signal morphology into the ADAPT modeling of the far-side magnetic flux distribution; however, its use may be limited. For instance, there is some noticeable spread in the tilt comparison in Figure 32. It may be useful to default to Joy's Law if, for instance, if the ellipse fit is poor or the phase signal area is below a threshold. The relationship between the observed magnetic area and GONG near-side phase area for active regions, depicted in Figure 31, reveals that the size of a far-side region can potentially be estimated accurately.

### 4.6.3 Testing and Application of ADAPT

ADAPT maps were used in the development of a brand new, unique, and highly promising method for forecasting solar EUV. In addition, the WSA coronal and solar wind model was significantly modified so that it could readily incorporate ADAPT maps in it.

#### 4.6.3.1 ADAPT EUV/XUV/FUV Forecasts

As an example of a direct space weather application using the ADAPT model, a new method for forecasting solar XUV (X-ray Ultra-Violet: 1-30 nm), EUV (Extreme Ultra-Violet: 30-120 nm), and FUV (Far ultra-Violet: 120-200 nm) variability was tested during the summer as a Philips Scholar project. The method is an expansion of the method developed the previous year to forecast the solar 10.7 cm (2.8 GHz) radio flux, abbreviated F10.7, utilizing advanced predictions of the global solar magnetic field generated by ADAPT. Using indices derived from the absolute value of the solar magnetic field, A good correlation was found between the observed mid-strength photospheric magnetic activity (field strengths between 25 and 150 G; referred to as "plage") and the observed UV values. As with the previous F10.7 forecast method ([31]), by evolving solar magnetic synoptic maps forward 1-7 days, the new method provided a realistic estimation of the Earth-side solar magnetic field distribution used to forecast UV.

For the Philips Scholar project, empirical models were developed using ADAPT magnetic flux sums to estimate measurements within select XUV/EUV/FUV bands. ADAPT's measurements of weighted photospheric magnetic sums for the active sunspot regions, or SA, and the photospheric magnetic plage regions, or SP, were used to form the empirical models. The best fit coefficients of these models were determined using the daily measurements made by NASA's Solar EUV Experiment (SEE) on the Thermosphere Ionosphere Mesosphere Energetic and Dynamics (TIMED) mission. The coefficients were estimated by fitting the models to approximately nine years (Feb. 8, 2002 to Dec. 30, 2010) of UV irradiance as measured by TIMED/SEE. For near-future applications with atmospheric models, the irradiance data are divided into the 37 Stan Bands [39], where the complete list is featured in Table 1. An example scatter plot between the ADAPT model and observations for Stan Band-9 is shown in Figure 33. The fitting method was then repeated to forecast UV irradiance using the same modeling technique on magnetic flux sums, SA and SP, for ADAPT forecast maps 1, 3, and 7 days in advance.

**Table 1. Table of Stan Band wavelength ranges, where bands 1-6 (purple) = XUV (soft x-ray), 7-26 (black) = EUV (extreme ultraviolet), & 27-37 (green) = FUV (far ultraviolet). Note that the He II 30.4 nm (304 Å) transition line is contained in Stan Band 9, and the Lyman alpha 121.6 nm (1216 Å) transition line is Stan Band 26.**

#	Wavelengths	#	Wavelengths	#	Wavelengths	#	Wavelengths
<b>1</b>	0.1-0.4nm	<b>11</b>	54.0-65.0nm	<b>21</b>	98.7-102.7nm	<b>31</b>	140.0-145.0nm
<b>2</b>	0.4-0.8nm	<b>12</b>	65.0-79.8nm (low)	<b>22</b>	102.7-105.0nm	<b>32</b>	145.0-150.0nm
<b>3</b>	0.8-1.8nm	<b>13</b>	65.0-79.8nm (high)	<b>23</b>	105.0-110.0nm	<b>33</b>	150.0-155.0nm
<b>4</b>	1.8-3.2nm	<b>14</b>	79.8-91.3nm (low)	<b>24</b>	110.0-115.0nm	<b>34</b>	155.0-160.0nm
<b>5</b>	3.2-7.0nm	<b>15</b>	79.8-91.3nm (mid)	<b>25</b>	115.0-120.0nm	<b>35</b>	160.0-165.0nm
<b>6</b>	7.0-15.5nm	<b>16</b>	79.8-91.3nm (high)	<b>26</b>	121.6nm Lyman- $\alpha$	<b>36</b>	165.0-170.0nm
<b>7</b>	15.5-22.4nm	<b>17</b>	91.3-97.5nm (low)	<b>27</b>	120.0-125.0nm	<b>37</b>	170.0-175.0nm
<b>8</b>	22.4-29.0nm	<b>18</b>	91.3-97.5nm (mid)	<b>28</b>	125.0-130.0nm		
<b>9</b>	29.0-32.0nm	<b>19</b>	91.3-97.5nm (high)	<b>29</b>	130.0-135.0nm		
<b>10</b>	32.0-54.0nm	<b>20</b>	97.5-98.7nm	<b>30</b>	135.0-140.0nm		

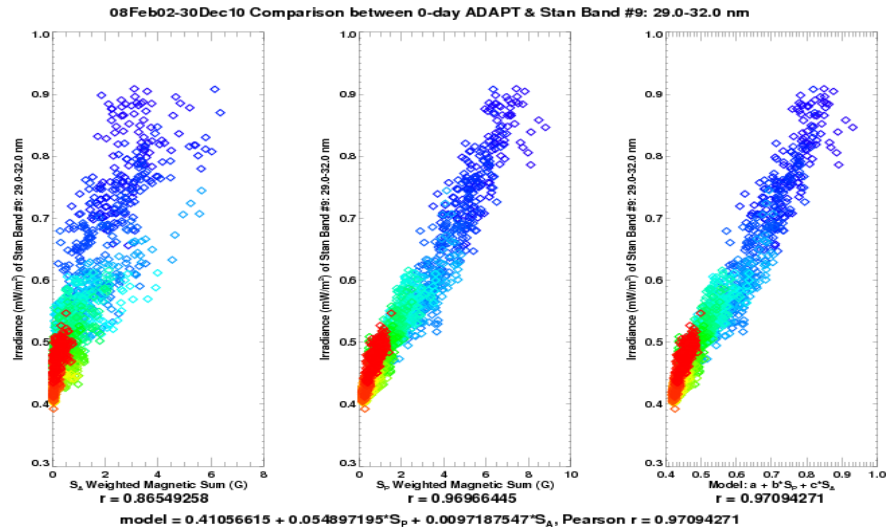


**Figure 33 .Comparison between ADAPT model and Stan Band-9 (29-32 nm). The active region weighted magnetic flux sum,  $S_A$ , is calculated using photospheric magnetic flux measured at or above 150 G. The plage region weighted magnetic flux sum,  $S_p$ , is calculated using photospheric magnetic flux measured between 25 G and 150 G. Color in this figure corresponds to time periods, where dark blue = 2002-2003 and red = 2010.**

In Figure 34 the ADAPT forecasted UV for Stan Band-9 is plotted along with the observed values for a six month timespan close to solar maximum, August 1, 2003 - February 1, 2004. The predicted values follow the observed trend very well, though there is a notable offset. Fortunately, the 0-day difference between prediction and observation can be applied to remove the bias for 1-day, 3-day, and 7-day forecasts. This timespan contains the October 2003 “Halloween” storms, shown as the central peak. The “Halloween” storm period was an unusual flaring period, so the fact that these forecasts under-predict this activity is not surprising since the model forecasts the background levels rather than flaring events. Using the modified forecast (Modified SD) models, by applying the 0-day difference between prediction and observation, to make the 1-7 day predictions results in excellent agreement with observation. The correlation

between observation and forecast for each Stan Band is show in Figure 35. Note that the 0-day correlation values (the “x” symbols) in Figure 35 are artificially set to a value of 1. Work comparing the irradiance behavior of TIMED/SEE with other instruments has started to better understand the Stan Bands 11 – 13 and the source of the lower correlation values. In addition, future goals include running ionosphere-thermosphere models using observed and forecasted UV values to compare results with the nominal methods still using F10.7 as input.

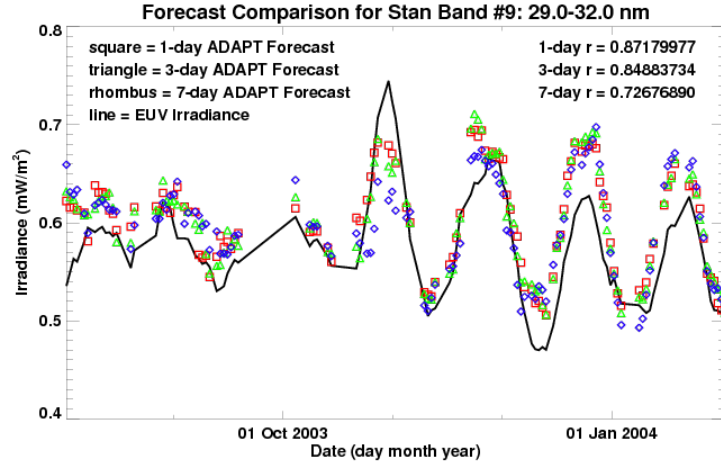


**Figure 34. Comparison between ADAPT combined model forecasts for the Stan Band-9 and the observed values. The Pearson correlation values are only for this period. This period contains the October 2003 “Halloween” storms (near the central peak) and was an unusual flaring period, thus a challenging period since the ADAPT model can only predict background levels rather than flaring events themselves.**

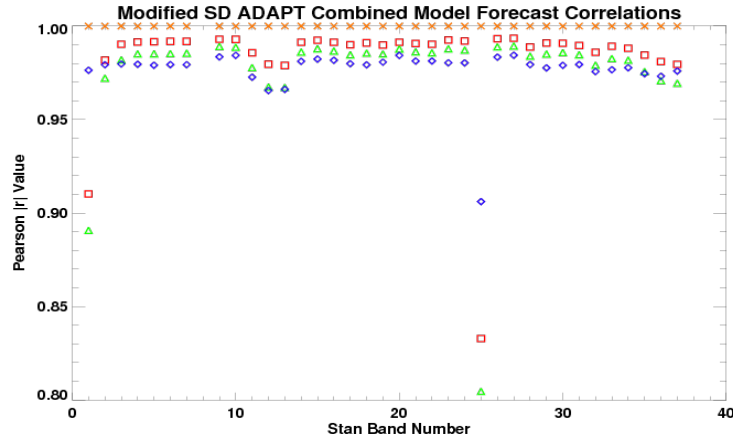


**Figure 35. Correlation values for each Stan Band between the ADAPT 1-day (red square), 3-day (green triangle), and 7-day (blue diamonds) and the UV observed values, for the period: 8 Feb, 2002 to 30 Dec, 2010. Except for Bands 1 (not actual observation) and 25 (poorly calibrated; Lyman-alpha wing not removed), the 1-7 day forecasts have correlation coefficients above 0.96.**

#### 4.6.3.2 Integration of ADAPT into WSA

Due to the complexity of the ADAPT model output files, significant changes to WSA were required to make it compatible with them. For example, unlike nearly all other photospheric magnetic field sources, the global ADAPT maps are in latitude-longitude format, as opposed to the more traditional sine-latitude-longitude format. This unique feature of ADAPT required that

a key module (and associated subroutines) within WSA be changed. Originally, the module simply assumed all observatory input maps were in sine-latitude format and automatically converted them to the WSA required latitude format. The module was changed so that it now checks the format of the observatory input files first and skips the sine-latitude to latitude conversion step when the maps are already in latitude. The WSA code was also changed so that it now routinely adds a standard key word to the headers of all observatory input maps indicating which format (sine-latitude or latitude) they are in.

Another complicating aspect of the ADAPT model output files is that they are comprised of an ensemble of global photospheric field maps (or realizations), as opposed to the more traditional one global map per observatory input file. Each ADAPT file also includes a binary table specifying the model parameters used to generate ensemble set of maps. WSA therefore had to be modified to accommodate these unique features of ADAPT, while also retaining its ability to ingest the file formats from solar observatories that it is already designed to work with. The approach decided upon for WSA is to keep the ADAPT realizations and associated binary table together, as a unit, in each of the (several) intermediate files generated by the code until it reached the stage in the program where the coronal solutions are run on the individual global maps (realizations). At this stage, the code runs a separate coronal solution for each individual ADAPT map and then saves the output as a separate file with the realization number being added to the file name to distinguish it from the other ensemble members. The WSA output files used to drive Enlil are also generated as individual files (i.e., one file per model realization) with the pertinent binary table stored in each of them.

In addition to the changes described above, it was also decided to radically change the file naming convention used by WSA. For more than a decade, WSA files were named using the following general convention:

file type (int = interpolated, wsa=coronal solution, etc), Carrington rotation number, longitude of the leading edge of the map, version number, and observatory name.

For instance, wsa\_2071\_289.00\_01\_gong.fits corresponds to the coronal solution output map having a leading edge with Carrington Rotation (CR) number and longitude coordinates of 2071 and 289.00 degrees, respectively, and version number 01, which indicates that it is the first map generated with this particular combination of CR number and longitude. If subsequently another map happens to be created that has exactly the same combination of values, the code knows to increment its version number to 02 and so on.

While rational, this naming convention has always made it hard to easily sort the WSA files in order of time, since Carrington longitude decreases with time. Also, one needs to be comfortable thinking in terms of CR number and longitude and also converting them to standard time. To simplify all this, a new file naming convention based on time was developed. The new system uses the following general convention:

file type name (int = interpolated, wsa=coronal solution, etc), year, month, day, hour, minute, realization number, and observatory name.

For instance, wsa\_200501161803R009\_ans.fits corresponds to the coronal solution output file (wsa) using the ADAPT NSO/VSM input map (ans) corresponding to a time and date of 18 hours and 3 minutes on January 16, 2005. R009 corresponds to the 9<sup>th</sup> realization of the ensemble set of model maps.

## 4.7 Year 7

The research effort in year seven focused on two main areas:

1. Further development and improvement in the ADAPT data assimilation methodology:
  - a) Seed map generation automated in ADAPT.
  - b) Improvement in ADAPT's localized ensemble transform Kalman filter (LETKF) methodology by including active ensemble inflation and adjustable ensemble size.
  - c) New LETKF data assimilation method compared to older techniques used in ADAPT.
2. Application of ADAPT maps:
  - a) Further development of a unique method for forecasting solar EUV/XUV/FUV.
  - b) Facilitated the incorporation of ADAPT EUV forecasts into ionospheric and thermospheric models.
  - c) Global impact of far-side flux emergence on coronal and solar wind models.
  - d) ADAPT driven time-dependent modeling of the solar wind using WSA+Enlil.
  - e) Advanced modeling of the solar corona using ADAPT.

### 4.7.1 Improvement in the Data Assimilation Methodology Used in ADAPT

Further development of the data assimilation capabilities for the Air Force Data Assimilative Photospheric Transport (ADAPT) model was carried out in year seven. A localized version of ensemble Kalman filtering was implemented in ADAPT. The Kalman filtering aspect of this process permitted approximation of the Worden-Harvey (WH) model's (i.e., the magnetic field flux transport component used within ADAPT) spatial covariance structure to effect the assimilation of new observations. At the same time the localization in the data assimilation eliminated erroneous long distance correlations occurring from the small sample sizes used to estimate the WH model's covariance structure. These improvements led to changes in ADAPT's handling of input parameters, which allowed the parameter space of the data assimilation routines to be studied more easily.

Routines, written in Python, were added to the ADAPT package which allowed for the generation of Seed Maps during runtime. These are maps of the Solar photosphere that have been perturbed to initialize the ADAPT ensemble. Automatic generation of Seed Maps allowed the effects of ensemble size on the ADAPT forecast to be studied. By increasing the ensemble size, the range of forecasts explored by ADAPT's flux transport routines was expanded. This led to a higher probability of including observations within this range, which improved the functionality of the data assimilation routines.

ADAPT's data assimilation ability was also expanded to include a localized ensemble transform Kalman filter (LETKF). This capability had already been included in ADAPT, but the routine was written in Fortran while the rest of ADAPT's structure was implemented in C. The new LETKF routine was rewritten into C and has the advantage of separating the actual data assimilation step and the localization of observations step into two separate functions. This allowed other routines that rely on an ensemble Kalman filter, but do not require localization, to be implemented quickly. Also, putting the localization routine into its own function allows one to examine the effects of different localization routines quickly.

Changes were also made to the specific way ADAPT handles inflation of the ensemble during data assimilation. Previously, the inflation parameter was exclusively used to adjust the weight of the covariance properties of the background ensemble. Now the inflation parameter perturbs the actual members of the background ensemble and the ensemble observations around their mean. This has the effect of making the propagating ADAPT ensemble explore a much wider range about its mean value which in turn lends greater weight on the photosphere observations during assimilation.

The main difference between the LETKF data assimilation implementation and the older ensemble least squares (ENLS) data assimilation schemes used is how much the ADAPT ensemble is adjusted to agree with the observations. With the ENLS, the spatial correlation structure of the ADAPT ensemble is not taken into account. This causes observations to be trusted far more than the ADAPT model forecast and therefore the ADAPT forecast is nearly discarded during the ENLS assimilation. In sections of the observation region near the central meridian, where observational noise is low, this can be acceptable. However, near the limbs of the observation region noise is considerable and discarding the model forecast is not desirable, see Figure 36.

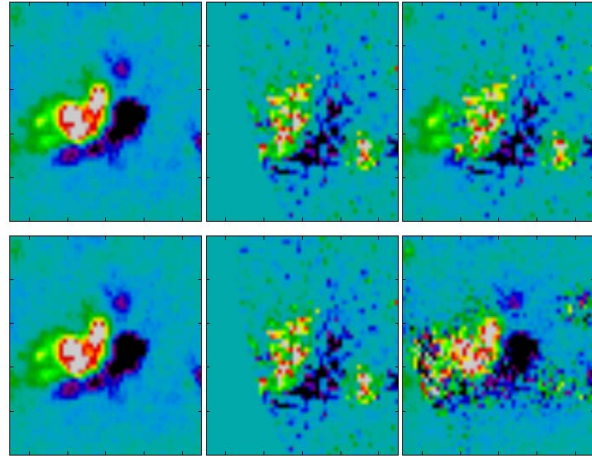


**Figure 36.** One assimilation step using ENLS assimilation (top row). Bottom row utilizes LETKF. The first column is the mean forecast, second column is the observation, and the last column is the analyzed ADAPT ensemble mean. The ENLS algorithm performs a pixel-by-pixel assimilation and therefore ignores spatial correlations in the ensemble. This leads to discarding the ADAPT ensemble forecast in favor of the observations. Since the LETKF takes into account local spatial correlations large structures, such as this active region, are preserved more.

The ENLS data assimilation that ADAPT used in the past suffers from the opposite problems that hinder the ETKF. With the ENLS observations are assimilated into the ADAPT ensemble pixel by pixel without ever taking sampled spatial correlations into account. Only pixel-wise standard deviations are considered, resulting in local distortion of coherent structures, such as large active regions, in the photospheric magnetic flux present in the ensemble. This is due to noise in magnetic flux observations that is not spatially correlated and therefore reduces spatial correlations in the observation. Overall the result of the ENLS data assimilation is to give little weight to the model ensemble information within the observation region thus reducing the information gained by including the Worden-Harvey model for photospheric flux transport. By observing one assimilation step, one can see how the ENLS assimilation favors observed magnetic flux over the ensemble model structure. In Figure 36 the ENLS data assimilation step eliminates the shape of the active region in its analysis ensemble whereas the LETKF blends the information from the Worden-Harvey model and the observations, maintaining the structure of the active region.

Another previously implemented assimilation method for ADAPT is the ensemble transform Kalman filter (ETKF), which makes use of an ensemble of complete (as opposed to local) model realizations when performing data assimilation. In situations, such as Solar photosphere models, where the dimension of the simulation state space is high, small ensemble size will give rise to spurious correlations. In the case of the solar photosphere these occur over long distances and thus severely restrict the analysis ensemble's pixel-wise standard deviation both near and far away from observations.

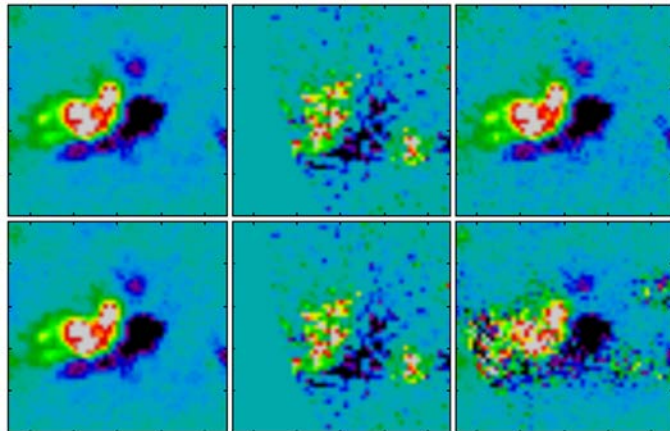


**Figure 37. One step of the ETKF assimilation (top row). The bottom row is one step of the LETKF assimilation. The columns are the same as in Figure 36. We can see that the ETKF essentially ignores the observation while the LETKF blends the observation and forecast ensemble.**

The local ensemble transform Kalman filter (LETKF) implemented in year seven only compares each pixel's observation with a model ensemble of nearby pixels. This eliminates the propagation of strong correlations over long distances due to the small ensemble size. The main effect of the variance reduction which occurs when the ETKF is used, in terms of accuracy of the data assimilation, is how much the observations are taken into account when adjusting the photosphere ensemble. The contrast is highlighted by observing one assimilation step for a large active region using the two methods, see Figure 37. The mean shape of the active region is

almost unaffected by the observations for the ETKF but is noticeably influenced by observations when the LETKF is utilized.

The ADAPT framework, using the LETKF with adjustable ensemble size and active ensemble inflation, does a noticeably better job at balancing the spatial propagation of information away from the point of observation than previous data assimilation methods. Ensemble Kalman filtering, as opposed to ensemble least squares filtering, also preserves the variance in the ensemble near data much more than the original ENLS assimilation. This allows for a more diffuse model forecast in regions where observations have not yet been made which increases the chance of the ensemble range capturing the true photospheric flux in these regions.

The advancements to ADAPT's data assimilation capabilities are detailed in [40]. Work was planned to develop methods of separating the assimilation of solar observations by the scale of structures present in observation and model. This would allow more trust to be put on observations of large emerging active regions of the photosphere that the underlying model does not forecast well. The addition of a robust assimilation routine for handling emergence of large active regions near the solar limbs would improve considerably the forecast of the photospheric flux which acts as a driving boundary condition for the corona and solar wind.

## 4.7.2 Application of ADAPT maps

### 4.7.2.1 Further Development of a Unique Method for Forecasting Solar EUV/XUV/FUV

As discussed in the year six annual report, a promising new method was being developed that makes use of ADAPT output to forecast the solar irradiance of selected wave-length ranges within the extreme ultraviolet (EUV) and far ultraviolet (FUV) bands. The technique is similar to the method Henney [31] developed to predict solar 10.7cm (2.8 GHz) radio flux, abbreviated F10.7, utilizing advanced predictions of the global solar magnetic field generated by the ADAPT photospheric flux transport model. In the last year of this effort, this EUV and FUV forecasting technique was further developed and refined and, as with the previous radio flux comparison, a good correlation was found between the absolute value of the observed photospheric magnetic field and selected EUV/FUV spectral bands. By evolving solar magnetic maps forward 1 to 7 days with a flux transport model, realistic estimations of the Earth-side solar magnetic field distribution are generated to forecast irradiance. For example, Pearson correlation coefficient values of 0.99, 0.99, and 0.98 are found for 1, 3, and 7 day predictions, respectively, of the extreme ultraviolet band from 29 to 32 nm. For the Lyman-alpha line (121.6 nm), on the EUV/FUV spectral border, correlation values of 1.0, 0.99, and 0.98 are found for 1, 3, and 7 day predictions, respectively. In the far ultraviolet, for example the 160 to 165 nm spectral band, correlation values of 0.98, 0.97, and 0.96 are found for 1, 3, and 7 day predictions, respectively. In [31], the observed F10.7 cm signal is found to correlate strongly with strong magnetic field (i.e., sunspot) regions, whereas the weak field (i.e., plage) regions are only needed to capture the solar cycle background component. It was found that observed integrated full-disk solar EUV and FUV signals are strongly correlated with the weaker magnetic fields associated with plage regions, suggesting that solar magnetic indices may provide an improved indicator (relative to

the widely used F10.7 signal) of EUV and FUV non-flaring irradiance variability as input to ionospheric and thermospheric models. This work was published in [41].

#### 4.7.2.2 Facilitating the Incorporation of ADAPT EUV Forecasts into Ionospheric and Thermospheric Models

The FUV/EUV/Soft X-ray portion of the solar spectrum constitutes the majority of energy input to the Ionosphere-Thermosphere (I-T) system and is responsible for the bulk of all heating and photochemical processes. Work with aim to drive an I-T General Circulation Model (GCM) with direct observations and ADAPT forecasts of irradiance over the relevant portion of the solar spectrum began in year seven (2014) of this project. Previous efforts to model these processes have relied on solar proxies (i.e., solar irradiance signals such as F10.7 that do not interact with the atmosphere and can therefore be monitored from the ground regularly) to specify variations in the FUV/EUV/Soft X-ray spectrum that interact strongly with the I-T. This method enforces the assumption that each band of the solar spectrum can be linearly mapped to the variations of the proxy. Analysis of TIMED-SEE and SDO-EVE data show significant spread of the FUV/EUV/soft X-ray data relative to the linear-proxy approximation, implying that this assumption is unjustified and can lead to errors in current-epoch and forecast GCM simulations.

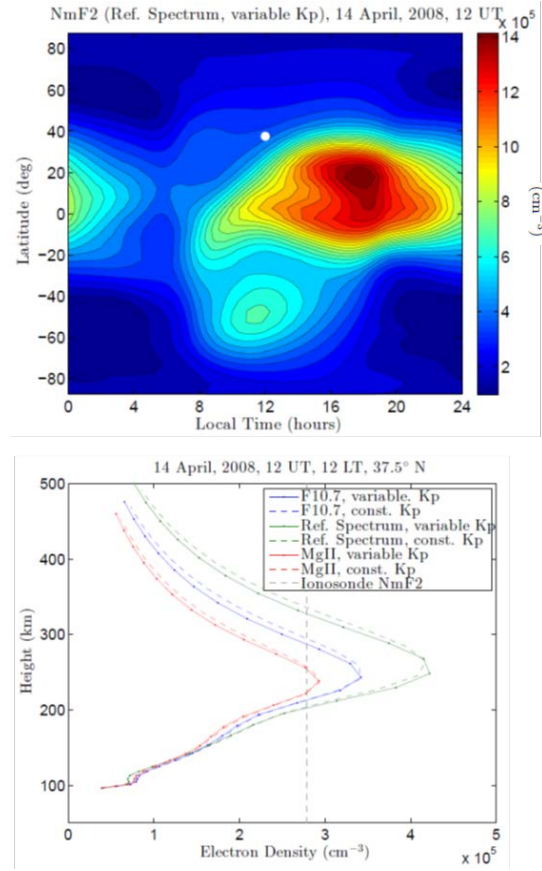


**Figure 38. Global F-peak electron density simulated by NCAR-TIEGCM (top) driven by the WHI interval spectrum. Bottom: Vertical profile of electron density at the Roquetes ionosonde as simulated by NCAR-TIEGCM driven by the WHI interval reference spectrum (green), F10.7 proxy (blue), and MgII proxy (red). Vertical grey line gives the F-peak density measured at Roquetes, Spain (lat=40.8°N, lon=0.5°E).**

As a first step, a method was implemented to ingest high-resolution solar irradiance data from a variety of sources into NCAR-TIEGCM. Potential sources include data from the TIMED-SEE and SDO-EVE instruments, well-validated solar minimum spectra such as those constructed during the Whole Heliospheric Interval (WHI), as well as forecast spectra from ADAPT predictions (see [41]). Consistent with [39], the selected high-resolution spectrum was integrated over wavelength-bins dictated by the variability in the atmospheric absorption cross-section of N2. This reduction is a necessary step, since running a GCM with a high-resolution (say 0.1 to 1 nm) spectrum at each grid point and time step would be computationally prohibitive. With the reduced high-resolution spectrum, TIEGCM's default proxy-based model, EUVACS, along with its associated pitfalls was bypassed.

Figure 38 shows an initial comparison between TIEGCM model simulations using the high-resolution solar minimum spectrum from the Whole Heliospheric Interval (WHI) as well as simulations using proxy-based specifications of solar irradiance such as EUVACS/F10.7 and EUVACS/MgII. As can be seen from the comparison between measured and modeled electron densities near the F-peak, use of the new high-resolution irradiance spectrum does not necessarily give an improvement in absolute accuracy. This is due mostly to the tuning that has occurred within the GCM over the years, in effect compensating for the proxy-based solar irradiance specification. Future efforts will focus more on the day-to-day variations that are induced in TIEGCM through the use of the new high-resolution spectrum methods, and less on the absolute accuracy. Eventually, TIEGCM may be re-tuned such that it tracks ionosonde and/or satellite drag data, depending on specific users' needs.

#### 4.7.2.3 Global Impact of Far-Side Flux Emergence on Coronal and Solar Wind Models

Although solar magnetic flux transport models, like ADAPT, can provide significantly improved estimates of the instantaneous state of the global photospheric magnetic field distribution, the success is greatly limited by the lack of input data from the far-side of the sun. With no past or planned space-based magnetographs to directly measure far-side solar magnetic fields, global maps often include data at least 15 days old. Section 4.5.1.2 described a case where a GONG helioseismically detected active region located on the far-side of the sun was assimilated into ADAPT. It was found that when this far-side active region was incorporated into the ADAPT maps and then used to drive WSA, it noticeably improved predictions of the corona and solar wind [34]. Over the last few years, it became increasing clear how significantly far-side activity can affect the global structure of the corona and thus solar wind. A concrete example of how critical it is to include far-side active region observations into a flux transport model like ADAPT is shown in Figure 39).

Figure 39b shows an ADAPT photospheric field map where a new magnetogram observation (gold-brown shaded region) was last assimilated into it on July 21, 2012. When this map is used to drive the WSA coronal and solar wind model, the solar wind predictions disagree significantly with in situ L1 spacecraft observations (see panel e in Figure 39). However, when the ADAPT map four days in the future (panel g) is used (thus including approximately 55° of longitude from the far-side), the agreement is remarkably improved (shown in panel j). Note that the poor agreement with observations from July 20-24 (see panel e and j) is very likely due to a sequence

of CMEs that occurred around that time (and not included in the WSA model). Over this four day interval several large active regions located between  $\sim 190$ - $240^\circ$  longitude have rotated onto the front side of the sun (i.e., the group in the middle of the map positioned just to the right of where the gold-brown region begins in panel 4g). While ADAPT evolved this part of the Sun since its passage behind the west limb  $\sim 14$  days prior, comparison of panels 4g with 4b reveal that new flux emerged during this time.

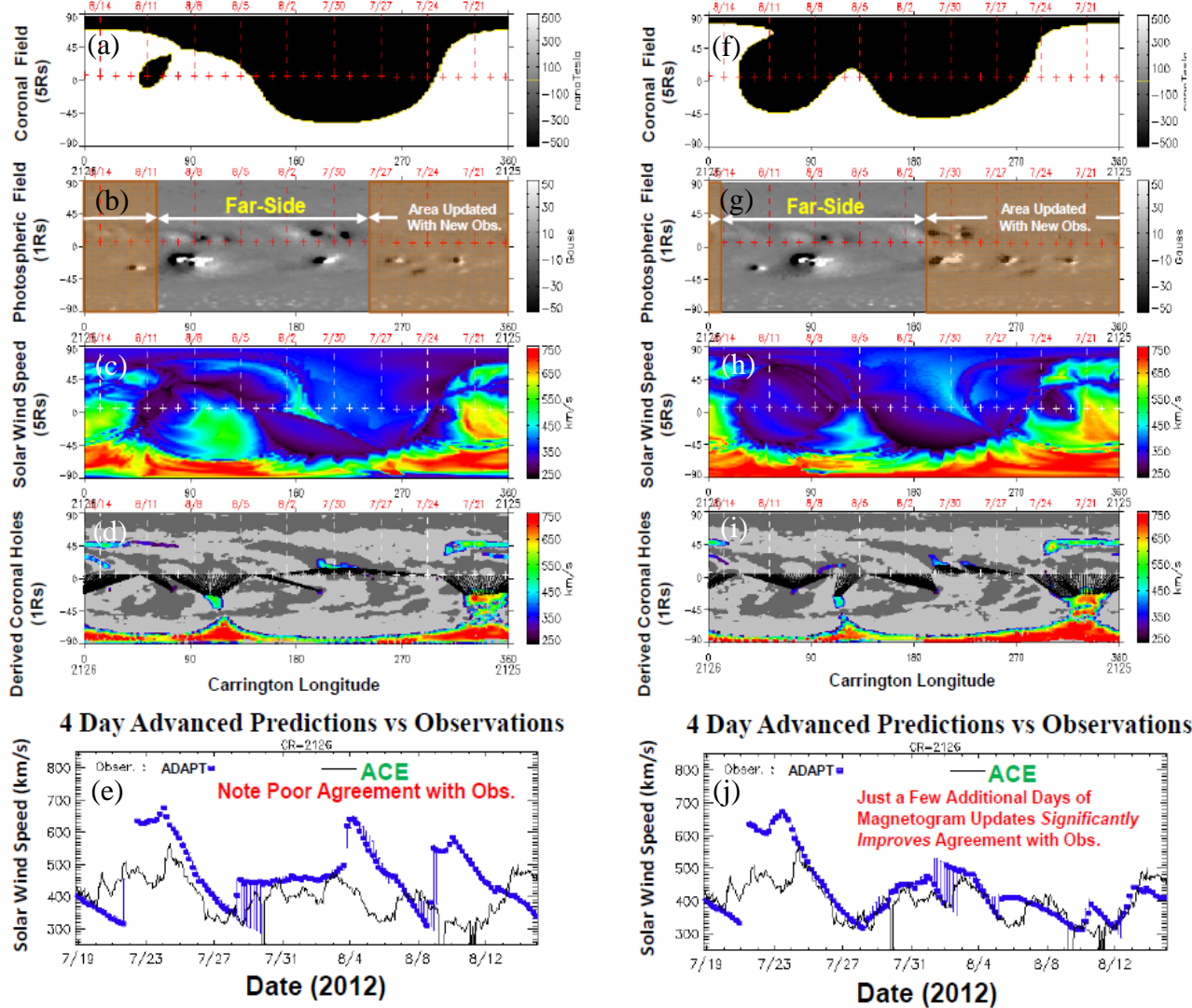


**Figure 39. WSA coronal and solar predictions driven by an ADAPT photospheric magnetic field map (left column). (b) Last updated with a GONG magnetogram on July 21, 2012, while the right column displays predictions for an ADAPT map updated 4 days later on July 25 (g). Panels a & f show the global coronal magnetic field polarity at  $5 R_s$ . Outward (Inward) directed field are indicated by white (black) areas. The red (or white in c, d, h & i) plus signs near the equator mark the daily positions of the sub-earth point. Panels c & h portray the solar wind speed at  $5 R_s$ . Panels d & i exhibit the modeled coronal holes, where the field polarity at the photosphere is indicated by the light/dark (positive/negative respectively) gray contours and the colored dots identify the foot-points of the open field lines at the photosphere. The dot color indicates the solar wind speed at  $5.0 R_s$  as predicted by the model. The black straight lines identify the connectivity between the outer (open field) boundary located at  $5.0 R_s$  and the source regions of the solar wind at the photosphere. Panels e & j depict the solar wind speed observations from ACE (black solid lines) vs. WSA predictions (blue dots) using ADAPT maps from, respectively, July 21 & 25, 2012.**

The effects of including the new flux are global, note that the coronal solutions (panels 39a and 39f) change significantly over these four days. In addition, the modeled solar wind speed (panels 39c and 39h) and coronal holes (39d and 39i) also change considerably. These global changes are physically too rapid and dramatic to have realistically occurred in such a short time span, but rather are a product of the model being updated “suddenly” with actual observations after more than 14 days. Including estimates of far-side active region flux distributions into ADAPT is thus critical for the modeling and forecasting the solar corona and wind. Although not shown here, the solar wind predictions at STEREO A & B (located approximately 120° behind and ahead of Earth’s orbital position at this time) also displayed similar dramatic improvement comparable to the L1 results. When this mere 55° wide complex of active regions is accurately represented in the ADAPT map, the model’s global description of the corona and solar wind is significantly improved.

It is thus demonstrated that far-side activity usually needs be incorporated into maps of the solar magnetic field distribution in order to adequately model the structure and properties of the global corona and solar wind. A major issue encountered and that needs to be addressed is how to more realistically incorporate far side activity into ADAPT. Over the last few years it was found that undetected far-side active regions that “suddenly” appear on the visible sun, or when far-side active region model estimates are inconsistent with that observed on the near-side, usually result in localized non-physical magnetic monopoles in global magnetic maps during the data assimilation process. Such artificial monopoles produce rapid, nonphysical changes in the time-dependent coronal and heliospheric model solutions (such as those discussed in the next two sections) taking hours to days for these artifacts to propagate out of the model grid.

#### **4.7.2.4 ADAPT Driven Time-Dependent Modeling of the Solar Wind Using WSA+Enlil**

In 2013 work began to do time-dependent WSA+Enlil runs using ADAPT maps as its driver. While ADAPT maps have been test in the WSA+Enlil model in the past, all previous cases, the model driven to steady state using a single (i.e., non-updating) map. In the final year of this effort, the model was driven with a continuously updating ADAPT photospheric magnetic field boundary condition. As a first test, a 60 day, 2 hour cadence time sequence of ADAPT maps (produced using GONG magnetograms) was generated for the February 15-April 15, 2012 time interval. The WSA+Enlil model was then driven using this set of ADAPT data. The results for the month of March are shown in Figure 40. Figure 40a (i.e., left panel) shows solar wind density model results in the ecliptic plane for March 1, 2012 at 0UT. The Sun is located at the center of the image and the positions of the planets (out to Mars) and several other satellites such STEREO A & B are also indicated. Figures 40b-e compare predictions and observations at Earth of the solar wind radial velocity, density, temperature, and magnitude of the magnetic field, respectively. The red solid line in panels 5b-e are the ACE satellite observations. As it turns out there were several CMEs during March 2012 and the blue solid line in Figure 40b-e displays the WSA+Enlil results with simulated CMEs included. The blue dotted lines indicate the model results when no simulated CMEs were included in the run. Overall, the model results (with the simulated CMEs included) agree reasonably well with observations. However, the model does over predict the solar wind speed during the latter part of the run (i.e., March 21-29). Further investigation revealed that a far-side active region (not included in the ADAPT maps) was

approaching the east limb during this period and was likely affecting the WSA coronal solutions used to drive Enlil. Once the active region appeared on the front side of the Sun and was thus integrated into ADAPT, the model and observations resumed to be in good agreement.

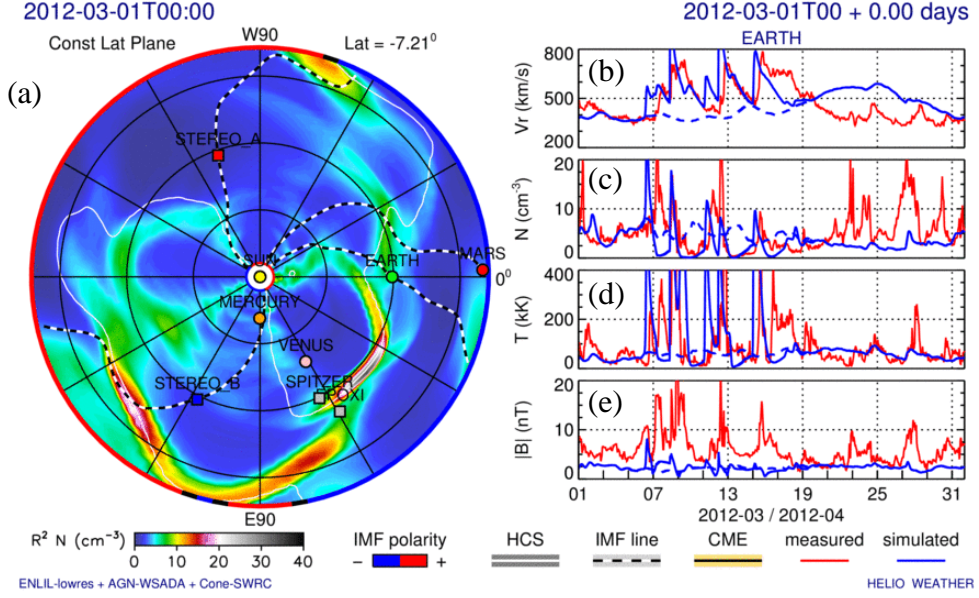


**Figure 40.** WSA+Enlil solar wind density in the ecliptic plane (a). (b-c) Comparison of simulated (blue) and observed (red) solar wind velocity, density, temperature, and the magnetic field magnitude at Earth. The blue dotted line seen in panels b-e are the WSA+Enlil results with no simulated CMEs included in the model. See text for additional details.

#### 4.7.2.5 Advanced Modeling of the Solar Corona Using ADAPT

Over the last few years the ADAPT team has been collaborating with scientists affiliated with Predictive Science Inc. (PSI) and RD/AFRL in a joint effort to incorporate into and test ADAPT maps in PSI's advance state-of-the-art 3-D MHD CORHEL coronal and solar wind model. In year seven (2014) significant progress was made in this area. Figure 41 shows an example of the new capabilities developed as a result of this work. The top row shows observed emission from the Atmospheric Imaging Assembly (AIA) instrument on board the Solar Dynamics Observatory (SDO) recorded emission on July 11, 2010 at 20:00. Note the active region near the east limb (left-hand side of the solar disk) and the extended coronal hole near disk center. The second row shows the simulated emission from CORHEL at moderate resolution using a Synoptic Optical Long-term Investigations of the Sun (SOLIS - magnetograph located at Kitt Peak Observatory, Arizona) synoptic map for Carrington Rotation (CR) CR2098. This is a standard run available with CORHEL at the start of this project. The third row shows a high resolution CORHEL MHD model computed using a high resolution ADAPT map for July 11, 2010. When the ADAPT map is used for the boundary condition of the simulation, an active region that emerged is visible in emission near the east limb, as is also seen in the observations. The extended coronal hole region near disk center in the high resolution model is thin and discontinuous, more closely resembling the observed coronal hole. These results appeared in the Fall 2014 HPC Insights quarterly magazine [42].

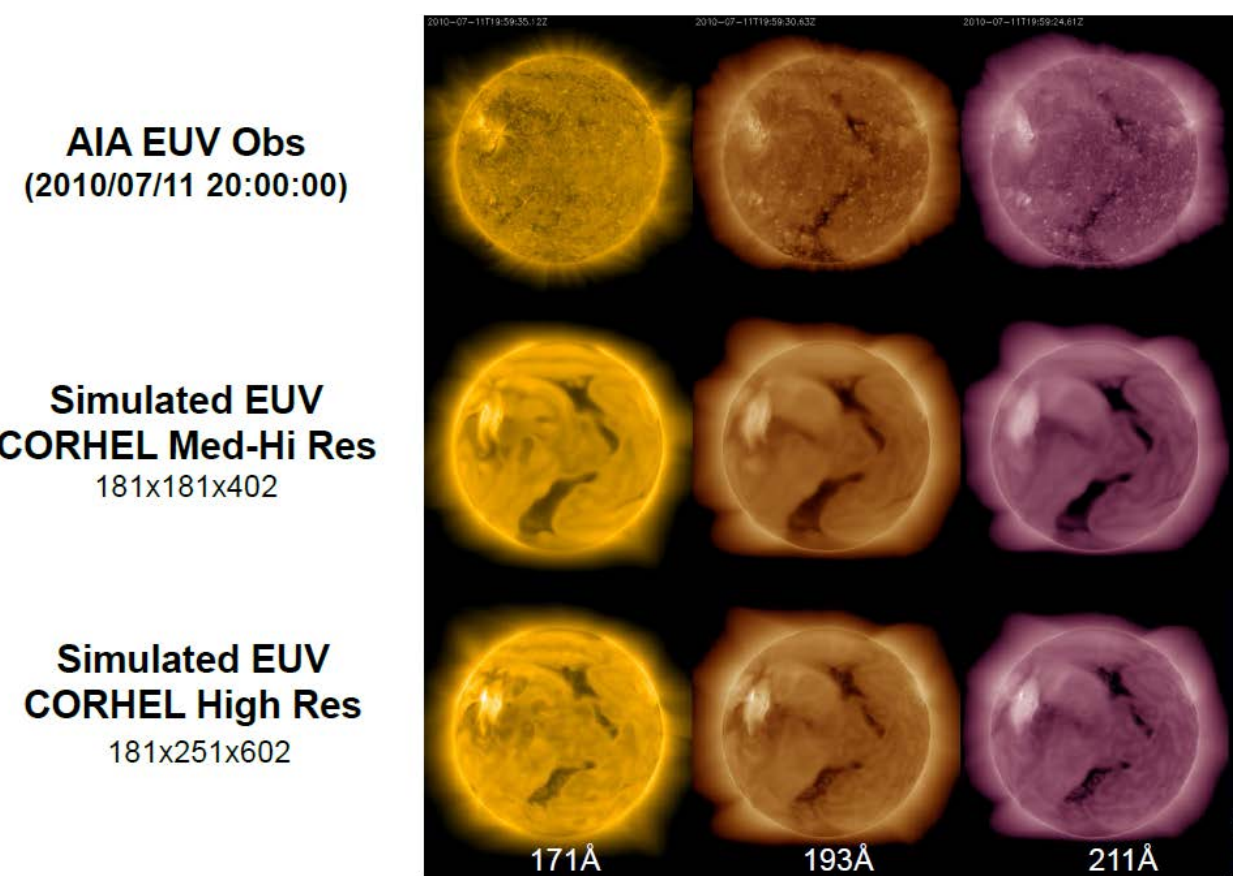


**Figure 41. Comparison of observed and simulated emission in the 171Å, 193Å, and 211Å lines of the AIA instrument aboard SDO. See text for additional details.**

Ultimately, the goal of this joint project is to drive the CORHEL model in a time-dependent manner using ADAPT maps. Year seven work on this effort revealed how truly important it is to provide temporally and spatially smooth descriptions of the global magnetic flux distribution required by CORHEL and all time-dependent models for that matter. Achievement of this will be a significant accomplishment resulting in more realistic and reliable forecasts of the corona and heliosphere.

## 5. CONCLUSIONS

The goal of this research effort was to improve significantly our ability to represent the instantaneous state of the global solar photospheric magnetic field distribution, which serves as the primary input to all coronal and solar wind models. The development of the Air Force Data Assimilative Photospheric flux Transport (ADAPT) model is the main outcome of this work. ADAPT is a photospheric magnetic flux transport model that makes use of rigorous data assimilation techniques. The transport model used in ADAPT is a highly modified version of the original Worden and Harvey model [6] developed at NSO. It evolves the solar magnetic flux by incorporating differential rotation, meridional drift, super-granular diffusion, flux cancellation, small scale random flux emergence transport processes during periods that lack observations for

a given solar region (e.g., such as on the far side of the Sun or at the poles). Updated data are incorporated into the model using the Los Alamos National Laboratory (LANL) data assimilation framework, which is an efficient and flexible data assimilation code that can apply, in order of increasing sophistication, the Least Squares (ENLS) estimation method, the traditional Ensemble Transform Kalman filter (ETKF) method, or the Local Ensemble Transform Kalman Filter (LETKF) method. In addition, a major aspect of this research effort was to develop methods for characterizing and incorporating helioseismic far-side active region data from NSO/GONG into the ADAPT model. Adding these unique and key measurements to ADAPT complements the earth-side magnetograms resulting in truly global solar photospheric field maps.

The relevance of the ADAPT model development is apparent through its increasingly broad application in both basic and applied solar, heliospheric, and space weather research. ADAPT maps have now been used in large number of coronal and solar wind models including CORHEL [43], WSA [25,29], Enlil [35], LEFM-Helio [44], University of Michigan Space Weather Modeling Framework (SWMF), the Magnetofrictional model [45], and Multi-Scale Fluid-Kinetic Simulation Suite (MS-FLUKSS) model [46]. The ADAPT global magnetic maps are helping to address questions regarding the structure and time evolution of the corona and solar wind; the evolution of coronal holes; the role solar magnetic fields play in radio and EUV/FUV emission; CME eruption, propagation, and evolution; the source regions of SEPs and the role that the background solar wind plays in their propagation; and the nature and evolution of the polar magnetic fields. Practical applications of ADAPT include its use as input to models used to forecast F10.7 radio emission, FUV and EUV irradiance, the corona, and the solar wind. In fact, at the time of the writing of this report, the plan is for the ADAPT model to soon be transitioned into operations at the National Centers for Environmental Prediction (NCEP) for both DoD (Air Force) and civil (e.g., NOAA) space weather forecasting purposes. The joint ESA/NASA Solar Orbiter mission also plans to use ADAPT maps in models that will help mission planners to decide where to point the spacecraft's instruments days in advance.

## References

- [1] Harvey, J., B. Gillespie, P. Meidaner, and C. Slaughter, "Synoptic solar magnetic field maps for the interval including Carrington Rotation 1601-1680, May 5, 1973 - April 26, 1979," *NASA STI/Recon Technical Report*, No. **81**, Aug 1980, pp. 21003.
- [2] Harvey, J. and J. Worden, "New Types and Uses of Synoptic Maps, Synoptic Solar Physics," *18th NSO/Sacramento Peak Summer Workshop held at Sunspot, NM, 8-12 September 1997, ASP Conference Series*, ed. by K. S. Balasubramaniam, Jack Harvey, and D. Rabin, **140**, Jan 1998, pp. 155-160.
- [3] Ulrich, R. K., S. Evans, J. E. Boyden, and L. Webster, "Mount Wilson Synoptic Magnetic Fields: Improved Instrumentation, Calibration, and Analysis Applied to the 2000 July 14 Flare and to the Evolution of the Dipole Field," *Astrophys. J. Sup.*, **139**, Mar 2002, pp. 259-279.
- [4] J. T. Hoeksema, "Structure and evolution of the large scale solar and heliospheric magnetic fields," Ph.D. Thesis, Stanford University, CA, Sep 1984.
- [5] Wang, Y.-M., N. R. Sheeley, Jr., and A. G. Nash, "Magnetic flux transport and the sun's dipole moment - New twists to the Babcock-Leighton model," *Astrophys. J.*, **375**, Jul 1991, pp. 761-770.
- [6] Worden, J. and J. Harvey, "An Evolving Synoptic Magnetic Flux map and Implications for the Distribution of Photospheric Magnetic Flux," *Solar Physics*, **195**, Aug 2000, pp. 247-268.
- [7] Schrijver, C. J. and M. L. DeRosa, "Photospheric and heliospheric magnetic fields," *Solar Physics*, **212**, Jan 2003, pp. 165-200.
- [8] Durrant, C. J. and J. McCloughan, "A method of evolving synoptic maps of the solar magnetic field, II. Comparison with observations of the polar fields," *Solar Physics*, **219**, Jan 2004, pp. 57-78.
- [9] Evensen, G., "The ensemble Kalman filter: theoretical formulation and practical implementation," *Ocean Dynamics*, **53**, Nov 2003, pp. 343-367.
- [10] Daley, R., "Atmospheric Data Analysis," Cambridge University Press, Cambridge, 1991.
- [11] Koller, J., Y. Chen, G. D. Reeves, R. H. W. Friedel, and T. E. Cayton, "Identifying the Radiation Belt Source Region by Data Assimilation," *Journ. Geophys. Res.*, **112**, Jun 2007, p. A06244, doi:10.1029/2006JA012196.
- [12] Lindsey, C. and D. C. Braun, "Helioseismic imaging of sunspots at their antipodes 1990," *Solar Phys.*, **126**, Mar 1990, pp. 101-115.
- [13] Lindsey, C. and D. C. Braun, "Helioseismic Holography," *ApJ*, **485**, Aug 1997, pp. 895-903.

[14] Lindsey, C. and D. C. Braun, “Seismic Images of the Far Side of the Sun,” *Science*, **287**, Mar 2000, pp. 1799-1801.

[15] González Hernández, I., F. Hill, and C. Lindsey, “Calibration of Seismic Signatures of Active Regions on the Far Side of the Sun,” *ApJ*, **669**, Nov 2007, pp. 1382-1389.

[16] Snodgrass, H. B., “Magnetic rotation of the solar photosphere,” *ApJ*, **270**, Jul 1983, pp. 288-299.

[17] Wang, Y.-M. and N. R. Sheeley, Jr., “The rotation of photospheric magnetic fields: A random walk transport model,” *ApJ*, **430**, Jul 1994, pp. 399-412.

[18] Mosher, J. M., “The magnetic history of solar active regions,” Ph.D. Thesis, California Institute of Technology, CA, 1977.

[19] Simon, G. W., A. M. Title, and N. O. Weiss, “Kinematic models of supergranular diffusion on the Sun,” *ApJ*, **442**, Apr 1995, pp. 886-897.

[20] Kalnay, E., “Atmospheric Modeling, Data Assimilation and Predictability,” Cambridge University Press, Cambridge, 2003.

[21] Bouttier, F. and P. Courtier, “Data assimilation concepts and methods March 1999,” Meteorological Training Course Lecture Series, ECMWF, 2002.

[22] Hunt, B.R., E.J. Kostelich, and I. Szunyogh, “Efficient Data Assimilation for Spatiotemporal Chaos: a Local Ensemble Transform Kalman Filter,” *arXiv:physics/0511236v2*, Nov 2005, pp. 1-32.

[23] Harvey, K. L., “Magnetic Bipoles on the Sun,” Ph.D. Thesis, Astronomical Institute, Utrecht University, 1993.

[24] Howard, R. F., “Solar Active Regions As Diagnostics of Subsurface Conditions,” *Ann. Rev. Astron. Astrophysics*, **34**, 1996, pp. 75-110.

[25] Arge, C. N., C. J. Henney, J. Koller, C. R. Compeau, S. Young, D. MacKenzie, A. Fay, and J. W. Harvey, “Air Force Data Assimilative Photospheric Flux Transport (ADAPT) Model,” *Solar Wind 12, AIP Conf. Series*, **1216**, Mar 2010, pp. 343-346.

[26] Odstrcil, D., V. J. Pizzo, and C. N. Arge, “Propagation of the 12 May 1997 interplanetary coronal mass ejection in evolving solar wind structures,” *Journ. Geophys. Res.*, **110**, Feb 2005, pp. A02106, doi:10.1029/2004JA010745.

[27] Harvey, J., D. Branston, C. J. Henney, and C.U. Keller, “Seething Horizontal Magnetic Fields in the Quiet Solar Photosphere,” *ApJ*, **659**, Apr 2007, pp. L177-L189.

[28] Arge, C. N., J. G. Luhmann, D. Odstrcil, C. J. Schrijver, and Y. Li, "Stream structure and coronal sources of the solar wind during the May 12th, 1997 CME," *JASTP*, **66**, Oct 2004, pp. 1295-1309.

[29] Arge, C. N., C. J. Henney, J. Koller, W. A. Toussaint, J. W. Harvey, J. W., and S. Young, "Improving Data Drivers for Coronal and Solar Wind Models," *ASTRONUM 2010, ASP Conference Series*, **444**, Oct 2011, pp. 99-104.

[30] González-Hernández, I., K. Jain, W. K. Tobiska, and F. Hill, "The far-side solar magnetic index," *J. Phys. Conf. Ser.*, **271**, Jan 2011, p. 012028, doi:10.1029/2012SW000767.

[31] Henney, C. J., W. A. Toussaint, S. M. White, and C. N. Arge, "Forecasting F10.7 with solar magnetic flux transport modeling," *Space Weather*, **10**, Feb 2012, pp. 2011-2019.

[32] Lionello, R., J. A. Linker, and Z. Mikić, "Multispectral emission of the Sun during the first whole Sun month: Magnetohydrodynamic simulations," *ApJ*, **690**, Jan 2009, pp. 902-912.

[33] Saint-Hilaire, P., G. J. Hurford, G. Keating, G. C. Bower, and C. Gutierrez-Kraybill, "Allen Telescope Array multi-frequency observations of the Sun," *Sol. Phys.*, **277**, Apr 2012, pp. 431-445.

[34] Arge, C., C. Henney, I. Gonzalez-Hernandez, W. Toussaint, J. Koller, and H. Godinez, "Modeling the Corona and Solar Wind using ADAPT Maps that Include Far-Side," *Solar Wind 13, AIP Conf. Series*, **1539**, Jun 2013, pp. 11-14.

[35] Lee, C. O., C. N. Arge, D. Odstrcil, G. Millward, V. Pizzo, J. M. Quinn, and C. J. Henney, "Ensemble modeling of CME propagation," *Solar Phys.*, **285**, Jul 2013, pp. 349-368.

[36] Godinez, H. C. and J. Koller, "Localized Adaptive Inflation in Ensemble Data Assimilation for a Radiation Belt Model," *Space Weather*, **10**, Aug 2012, p. S08001, doi:10.1029/2012SW000767.

[37] Wang, X. and C. H. Bishop, "A comparison of breeding and ensemble transform Kalman filter ensemble forecast schemes," *J. Atmos. Sci.*, **60**, May 2003, pp. 1140-1158.

[38] MacDonald, G. A., C. J. Henney, M. Díaz Alfaro, I. González Hernández, C. N. Arge, C. Lindsey, and R. T. J. McAteer, "Active Region Morphologies Selected From Near-Side Helioseismic Data," *ApJ*, **807**, Jul 2015, doi:10.1088/0004-637X/807/1/2.

[39] Solomon, S.C. and L. Qian, "Solar extreme-ultraviolet irradiance for general circulation models, Qian," *J. Geophys. Res.*, **110**, Oct 2005, pp. A10306, doi:10.1029/2005JA011160.

[40] Hickmann, K. S., H. C. Godinez, C. J. Henney and C. N. Arge, "Data Assimilation in the ADAPT Photospheric Flux Transport Model," *Solar Physics*, **209**, Apr 2015, pp. 1105-1118.

[41] Henney, C. J., R. Hock, A. Schooley, W. Toussaint, S. M. White, and C. N. Arge, “Forecasting Solar Extreme and Far Ultraviolet Irradiance,” *Space Weather*, **13**, Mar 2015, pp. 141-153.

[42] Williams, S., R. B. Duncan, J. Linker, C. Downs, R. Lionello, J. Wijaya, C. N. Arge, and C. Henney, “Advanced Solar Telescope Weather Modeling,” *DoD HPC Insights Magazine (Cover Story)*, Fall 2014, pp. 2-6.

[43] Linker, J. A., Z. Mikić, P. Riley, C. Downs, R. Lionello, C. Henney, and C. N. Arge, “Coronal and Heliospheric Modeling Using Flux-Evolved Maps,” *Solar Wind 13, AIP Conf. Series*, **1539**, Jun 2013, pp. 26-29.

[44] Merkin, V. G., J. G. Lyon, D. Lario, C. N. Arge, and C. J. Henney, “Time-dependent magnetohydrodynamic simulations of the inner heliosphere,” *Journ. Geophys. Res.*, 2016, in press.

[45] Weinzierl, M., A. R. Yeates, D. H. Mackay, C. J. Henney, and C. N. Arge, “A New Technique for the Photospheric Driving of Non-Potential Solar Coronal Magnetic Field Simulations,” *ApJ*, in press.

[46] Manoharan, P., T. Kim, N. V. Pogorelov, C. N. Arge, and P. K. Manoharan, “Modeling solar wind with boundary conditions from interplanetary scintillations,” *Journal of Physics, Conf. Ser.*, **642**, Sep 2015, p. 012016, doi:10.1088/1742-6596/642/1/012016 642.

## **DISTRIBUTION LIST**

DTIC/OCP  
8725 John J. Kingman Rd, Suite 0944  
Ft Belvoir, VA 22060-6218

1 cy

AFRL/RVIL  
Kirtland AFB, NM 87117-5776

2 cys

Official Record Copy  
AFRL/RVBXS/Dr. Charles N. Arge

1 cy